Neurally-Informed Models of Protracted Sequential Sampling of Long Noise-free Stimuli

Hadiseh Hajimohammadi[1], Kieran S Mohr[1], Redmond G O'Connell[2], and Simon P Kelly[1]

[1] School of Electrical and Electronic Engineering and UCD Centre for Biomedical Engineering, University College Dublin, Belfield, Dublin 4, Ireland;
[2] Trinity College Institute of Neuroscience and School of Psychology, Trinity College Dublin, Ireland

Correspondence: hadiseh.hajimohammadi@ucd.ie and simon.kelly@ucd.ie

Abstract

Sequential sampling models have provided a rich theoretical framework in the study of perceptual decision-making and quantitatively capture diverse behavioural data. However, research has increasingly highlighted that for the long-duration, statistically stationary stimuli commonly studied, it is difficult to definitively establish the operation of protracted sampling or temporal integration as opposed to non-integration strategies like extremum-detection, especially when based on behaviour alone. Here, we attempted to resolve such mechanistic details in the interesting case of judging subtle feature-differences (contrast) in a long (1.6-sec), noiseless stimulus, by jointly analysing the accuracy of delayed reports and the dynamics of a centroparietal electroencephalographic signal ('CPP') reflecting decision formation. Accuracy steadily increased across four covertly-manipulated evidence durations and the CPP remained elevated throughout the stimulus period, together indicating protracted sampling. Models fit to CPP dynamics as well as accuracy resolved more details than those fit to accuracy alone, such as the setting of a bound. However, a convincing joint neural-behaviour fit could be achieved not only by a temporal integration model, but also by an extremum detection model that evoked a stereotyped signal 'flagging' the first single-sample bound crossing. This illuminates interesting, testable alternatives to integration, and the limited extent to which combining neural decision dynamics with behavioural information can uniquely identify underlying mechanisms in some behavioural scenarios.

Introduction

Sequential sampling models based on the integration of evidence over time are very prominent in the study of perceptual decision-making (Gold & Shadlen, 2007). They provide an intuitive means to achieve optimal performance despite perceptual noise and to improve in accuracy given longer stimulus durations; they provide excellent fits to behaviour on diverse tasks (Ratcliff et al., 2016); and, with the addition of an action-triggering bound, they can explain the trade-off between speed and accuracy. (Heitz, 2014). Moreover, neural signals that exhibit the build-up dynamics predicted of an evidence-integrating "decision variable" have been found in rodents (Hanks & Summerfield, 2017) and non-human primates (Gold & Shadlen, 2001), and humans (O'Connell et al., 2012). The capability of the brain to perfectly integrate sensory evidence over long timescales (tens of seconds) has been demonstrated using expanded judgment tasks where evidence is provided in just a few discrete, highly stochastic tokens (Hyafil et al., 2023; Waskom & Kiani, 2018). However, in the case of the most typically studied perceptual decision tasks, which involve continuously presented, statistically stationary sensory evidence (e.g. dot-motion direction, contrast), the role of extended integration is the subject of continued debate. These tasks are very distinct from expanded judgment tasks in providing high-category information relatively immediately (Lange et al., 2021), and, accordingly, sensory information is often found to be strongly choice-predictive only over a restricted time range (Ludwig et al., 2005), even when long stimulus timeframes promise further gains in accuracy (Kiani et al., 2008). It has been argued that decision-makers may default to a restricted temporal window of integration because it best suits natural interactions with dynamic environments (Uchida et al., 2006), and that decision termination can be determined more by elapsed time than criterion levels of cumulative evidence (Thura et al., 2012). Even for the canonical perceptual decision task of dot-motion discrimination whose noisy nature would intuitively appear to require integration, it has been shown that an integration strategy cannot be taken for granted, with alternative non-integration strategies, such as extrema detection or intermittent evidence sampling, providing comparably good fits to most typical behavioural data patterns, including improvements in accuracy with duration and reduction of reaction time (RT) and error rate with increasing evidence strength (Stine et al., 2020). Thus, the scope of circumstances in which protracted integration underpins perceptual decisions is far from settled.

A major challenge in establishing the role and timeframe of temporal integration is that behavioural data derived from many typical experimental designs provide insufficient constraints to overcome problems of model mimicry, where data generated from one mechanism can be quantitatively explained equally well by another mechanism (Evans & Wagenmakers, 2020; Khodadadi & Townsend, 2015; Trueblood et al., 2021). A newly emerging strategy to overcome this is to constrain behavioural models with neurophysiological signals that reflect core processes in the model (O'Connell et al., 2018; Purcell & Palmeri, 2017). In humans, dynamically evolving signatures of decision formation and motor preparation have proven valuable in guiding and constraining decision models (Afacan-Seref et al., 2018; Corbett et al., 2023; O'Connell & Kelly, 2021). One such signal, the Centro-Parietal Positivity (CPP), exhibits many key properties expected of a theoretical decision variable: its buildup rate scales with evidence strength and it is coextensive with the decision period, in that its onset is time-locked to evidence onset while its peak is aligned to the behavioural response consistent with termination upon reaching a bound (Kelly &

O'Connell, 2013; O'Connell et al., 2012). Its buildup dynamics track perturbations in the evidence during decision formation, even in the absence of motor requirements, and it is present for any relevant sensory attribute forming the basis of a decision, but absent when the same attribute is irrelevant for any decision (O'Connell et al., 2012). Further, its amplitude co-varies with decision accuracy across conditions and reaction time quantiles (Kelly et al., 2021; Steinemann et al., 2018). Although a role in decision formation is clear, and all of these properties are consistent with a decision variable that specifically operates by temporal integration, it is far from certain that any task that elicits a CPP must therefore involve temporal integration. As was found to be the case for behavioural data (Stine et al., 2020), it is possible that non-integration strategies could viably generate similar average buildup dynamics in neural decision signals (Latimer et al., 2015). Indeed, simulations have shown that neural signals generated by different underlying mechanisms can exhibit similar features, demonstrating that the problem of model mimicry can extend to neurophysiological decision signals; however, by modelling behavioural and neural data together, the joint set of constraints can provide a stronger basis to resolve competing hypotheses about decision mechanisms, while also bolstering interpretations of the neurophysiological signals themselves (Purcell & Palmeri, 2017).

Here, we adopted this approach to address the question of whether extended sensory evidence sampling, and specifically temporal integration, underpins difficult perceptual judgements of relatively long-duration, noiseless stimuli with delayed reports. Specifically, we implemented a task in which participants judged which of two overlaid flickering gratings had higher contrast over a fixed 1.6-second stimulation period, reporting their choice after stimulus offset. This scenario represents an interesting borderline case for probing the role of protracted temporal integration because, on the one hand, the absence of noise in the physical stimulus would seem to minimise the benefits of time-averaging, while on the other hand, even a noiseless sensory feature, when subtle, would be vulnerable to internal neural noise in sensory encoding and could thus benefit from integration. Moreover, in previous studies examining delayed reports after long stimulus periods, it has been found that even with stimulus noise, decision makers do not seem to make use of the whole period but rather terminate their decision early, as expressed in limited accuracy improvements with stimulus duration (Kiani et al., 2008), and in decision signals reaching their peaks less than halfway through the stimulus period (Twomey et al., 2016). It is not clear whether this reflects a general tendency or capacity limitation, or the strategic setting of a low bound because there was relatively little to be gained by further sampling in those particular task circumstances. For example, high evidence strengths may mean that near-ceiling accuracy is achievable from only a short initial evaluation (Twomey et al., 2016), and in tasks with variable stimulus durations (Kiani et al., 2008), long-duration trials may be sufficiently rare as to not be worth catering for in one's decision policy. Here, we attempted to minimise any such strategic discounting of extended sampling by making low-evidence strength dominant (80% of trials) and manipulating evidence duration within the fixed stimulus period without the participants' awareness, by stepping the subtly-differing contrast levels back to equal baseline levels at a variable time. To ensure that we could probe decision bounds even if set high, we interleaved occasional (20%) trials with very high evidence strength.

We found that behavioural accuracy steadily improved with duration, including from 0.8 to 1.6 sec, and that the CPP remained elevated up to the end of the stimulus period, together indicating protracted evidence sampling. Behavioural accuracy across the five conditions, on its own, could be quantitatively well-captured not only by integration (drift-diffusion) but also

by a set of extrema detection models involving sequential sampling without integration, with neither model class able to definitively establish whether a decision bound is set. We devised two plausible mechanisms through which extrema detection could produce buildup dynamics in the average decision variable as well as the accuracy trends, through a continually-updating extremum-tracking process or through stereotyped signals 'flagging' bound-crossings. We found that whereas the extremum-tracking model could not satisfactorily capture CPP dynamics in addition to behavioural accuracy, the extremum-*flagging* model was comparable to the integration model in its ability to do so. Both model classes benefitted from the inclusion of a collapsing decision bound and/or starting point variability to achieve a good fit, evidence for which was also observed in empirical motor preparation signals. We go on to discuss the implications of this, including the contribution of immediate-response data to provide information on decision termination timing, and what might be required of such an extremum-flagging model in order to further explain such data.

Results

We recorded EEG from 16 human participants during a task where they viewed two oppositely oriented, overlaid gratings flickering in alternation. After a 1.2-sec baseline period of equal, 50% contrast, the gratings underwent an equal and opposite contrast change, and after an additional 1.6-sec stimulus-assessment period, participants reported by button press which grating had higher contrast. In 80% of trials, the contrast differential was small (±10%) and lasted for 0.2, 0.4, 0.8, or 1.6 sec before stepping back to equal contrast and ultimately disappearing at 1.6 sec. For the remaining 20% of trials, a trivially easy (±40%) contrast difference was presented for 1.6 sec, reinforcing the belief in a fixed evidence duration of 1.6 sec (Figure 1A).

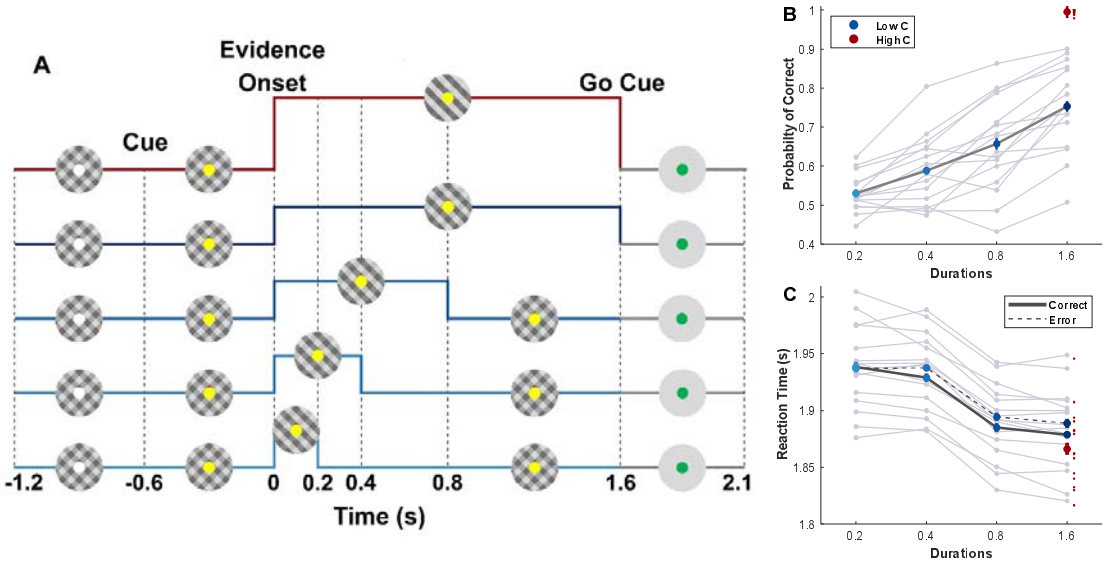

Figure 1. Contrast comparison task and behavioural results. (A) Stimulus and Evidence Time Courses: The stimulus consisted of two interleaved gratings flickering on and off in alternation, whose relative contrast had to be judged. 0.6-sec after achieving fixation and triggering stimulus onset, the fixation point turned yellow to cue participants to prepare for the onset of contrast-difference evidence another 0.6-sec later. In all trials, the stimulus remained on for a full 1.6 sec following evidence onset, after which it disappeared and the fixation turned green to prompt the subject to make a left/right-hand button press to indicate that the left- or right-tilted grating had higher-contrast, within a 0.5-sec deadline. In 80% of trials, a weak (±10%) contrast increment/decrement was oppositely applied to the

two gratings, lasting for 0.2, 0.4, 0.8, or 1.6 sec, returning to equal baseline contrast for any remaining time until stimulus offset. In the remaining 20% of trials, an easy contrast increment/decrement of ±40% was applied for the entire 1.6-sec period. (B) Accuracy significantly increased with the duration of the stimulus for low-contrast trials (blue dots) and was at the ceiling for the high-contrast condition (red dot). Individual participants' accuracies are shown in grey lines. (C) The mean reaction time (RT; relative to evidence onset) slightly decreased in trials with longer durations and higher contrast levels. Correct responses (solid, with individuals also shown in grey) were also slightly faster than error responses (dashed) in this delayed response task. For b and c, data are mean ± s.e.m. after between-participant variance was factored out.

Accuracy varied significantly across the five conditions (rmANOVA, F (4,60) = 150.47, p $<4.2 \times 10^{-16}$, Figure 1B) and increased with duration within the low-contrast conditions (rmANOVA, F (3,45) = 50.19, increasing trend p$<5 \times 10^{-11}$; all three consecutive duration pairs p<0.002; Table S1). Despite responses being deferred to stimulus offset, response time (RT) also significantly varied across conditions (rmANOVA F=12.35.31, p=2.15×10^{-7}), showing a mild downward trend with increasing duration in the low-contrast conditions (p$<2.48 \times 10^{-2}$), suggesting that subjects had not always reached commitment before the end of the stimulus period (Figure 1C; Table S2).

Models fit to behaviour only

Although steadily increasing accuracy over such a wide range of evidence durations seems suggestive of integration, increasing accuracy trends can also be produced by non-integration mechanisms (Stine et al., 2020). We thus began by comparing an integration model to two non-integration models in terms of their ability to capture this trend in accuracy. In all models, evidence samples were drawn from a normal distribution with a positive mean ("drift rate") during the evidence period and zero mean during the equal-contrast periods, with positive/negative values representing samples favoring the correct/incorrect alternative. What differs among these models is how the evidence is used to determine a decision in each model. Where applicable, variants of each model both with a constant bound and without a bound were implemented.

Integration

A variant of the drift-diffusion model was used as the integration model (Ratcliff & McKoon, 2008). In a bounded variant ('BIntg'), samples of momentary evidence were integrated perfectly over time (Figure 2A, top row, see Method for details) and decisions either terminated with a correct/incorrect choice upon reaching the appropriate bound or, if the bound was not reached by stimulus offset, decisions were determined by the sign of the cumulative evidence at stimulus offset. In an unbounded variant ('UIntg'), the choice was always determined by the latter mechanism (Figure 2A, top left). This scheme follows previous work with experimenter-controlled evidence-viewing durations (Kiani et al., 2008).

Extrema Detection

Extrema detection models were based on those introduced in previous studies (Hyafil et al., 2023; Stine et al., 2020; Waskom & Kiani, 2018), in which evidence is sampled sequentially but without any temporal integration, terminating in a correct/incorrect choice when the first sample exceeds the upper/lower bound (Figure 2A middle row). We considered three strategies to determine the choice in the absence of a bound crossing: either i) a random 50/50 guess was made (labelled 'BExtG' for bounded extrema detection with guess default), ii) the sign of the last sample determined the choice ('BExtL'), or iii) the sign of the most extreme (sub-bound) recorded sample determined the choice ('BExtE'). This last variant,

unlike the previous two, involves a memory component to retain the running extremum. Although memory is sometimes associated with integration in terms of potentially shared mechanisms (Wong & Wang, 2006), we class this variant as a non-integration model because the one remembered item (the most recent extremum) is updated sparsely and replaces rather than builds on the previous value, unlike integration which entails continuous, iterative updates. We refer to this as an 'Extremum-tracking' mechanism to distinguish it from the other two extrema detection variants. We also implemented an unbounded variant of this mechanism ('UExtE'), since, in making use of the full stimulus-assessment period, it has the ability to increase in accuracy with increasing evidence duration. Unbounded variants of the ExtG and ExtL models were not implemented because, in never reaching a bound by design, such models would always default to either guessing (ExtG) or being based on the very last evidence sample (ExtL).

Snapshot

In the Snapshot model, no integration or sequential sampling of evidence is involved; instead, it simply takes any random sample during the 1.6-sec stimulus-evaluation period and bases the choice on that sample (Stine et al., 2020). In the unbounded variant ('USpst'), the sign of the single sample determined the choice. In the bounded variant ('BSpst'), correct/incorrect choices resulted when the single sample exceeded the upper/lower bound, or from random guesses when a bound was not exceeded (Figure 2A, bottom row).

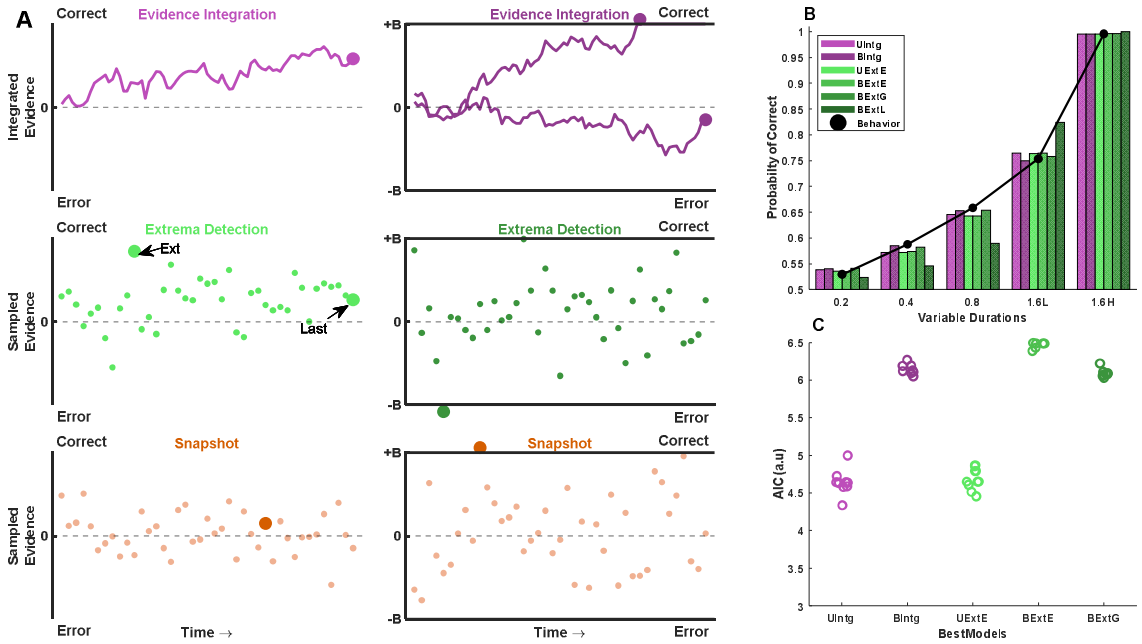

Figure 2. Alternative models and their fits to behaviour only. (**A**) Illustrations of Integration, Extrema Detection, and Snapshot mechanisms, including unbounded variants (left) and bounded variants (right). In the unbounded integration model (light purple), the sign of the accumulated evidence at stimulus offset determines the choice, while in bounded integration (dark purple), the decision is either terminated by reaching the correct or error bound or otherwise determined in the same way as in the unbounded model. In the unbounded Extremum-tracking model (light green), the decision is based on the sign of the evidence sample that attains the maximum absolute value. In the bounded Extrema detection model (dark green), a choice is determined as soon as a single sample exceeds a bound or, if neither bound is reached, the choice is determined by: i) a random guess (BExtG); ii) the sign of the

last sample (BExtL); or iii) the sign of the sample that attains the most extreme value (BExtE). Finally, the Snapshot model, where the choice is based on a single sample chosen at random (uniform distribution over time), is shown in the bottom row. In the unbounded version, the decision is made based on the sign of the sample. In the bounded version, the decision is based on whether the sample surpasses the bound; otherwise, the decision is guessed. (**B**) Observed (black dots) and model-predicted (bars) accuracy, showing that the five best-fitting models can capture the observed accuracy improvement with duration well. (**C**) AIC values across the 5 most competitive models show that models without bounds are favoured due to parsimony, and selection among integration and non-integration mechanisms is largely inconclusive. Given that we computed G^2 values through Monte-Carlo simulation, we conducted the fits with 10 different instantiations of noise, each shown here as a separate point. These clustered points depict the variability of the G^2 values due to the stochastic nature of these simulations, underlining how the small margins among the best models in Table 1 are inconclusive (see Methods).

We compared all of the above-mentioned models using the Akaike Information Criterion (AIC) based on a G^2 goodness of fit metric derived from behavioural accuracy. The drift rate was allowed to vary with evidence strength (two free parameters for the two contrast-difference levels) in the main versions of all models, but we also included single-drift rate variants (denoted '_1d') of the unbounded models to provide a worst-case benchmark for each mechanism. The results of these model fits are shown in Table 1.

Table 1: Goodness of fit metrics and parameter estimates of models fit to behaviour only. Models beginning with U were unbounded, and beginning with B were bounded, with the bound parameter denoted by B. Drift rates for low and high contrast difference were denoted by D1 and D2, respectively. G^2 quantifies how closely the model quantitatively fits the data, while Akaike's Information Criteria (AIC) adds a penalty for complexity. For both metrics, lower values indicate better fits. Colour shading highlights the competitive models depicted in Figure 2C.

Models		AIC	G^2	D1	D2	B
Snap Shot	USpst_1d	96.02	96.02	3.97	-	-
	USpst	36.31	32.31	2.0	8.1	-
	BSpst	39.4	33.4	2.0	9.06	0.00007
Integration	UIntg_1d	64.4	64.4	0.088	-	-
	UIntg	4.53	0.53	0.057	0.20	-
	BIntg	6.14	0.14	0.056	0.226	0.128
Extrema Detection	BExtG	6.17	0.17	10.3	11.65	0.034
	BExtL	21.25	15.25	1.41	6.96	0.017
	UExtE_1d	65.01	65.01	0.569	-	-
	UExtE	4.54	0.54	0.382	1.59	-
	BExtE	6.49	0.49	0.385	1.59	0.045

The drift rate for the high-contrast condition, was in all cases higher than for low-contrast as expected, and non-integration models generally needed much higher drift rates than integration models, simply because the same accuracies must be achieved based on one rather than many samples (Table 1; (Hyafil et al., 2023; Stine et al., 2020)). The snapshot models provided far poorer fits than the two sequential sampling models. The extrema detection model with last-sample default (BExtL) was also not competitive, because it predicts a disproportionate step-up in accuracy from the 0.8 to 1.6 sec duration where the

last sample becomes informative (Figure 2B). However, extrema detection models with a default guessing mechanism (BExtG) and with the extremum-tracking mechanism (UExtE and BExtE) fitted the data just as well as the equivalent integration models (Figure 2B,C). In the case of extremum-tracking, accuracy improvements with duration come from the fact that the longer the period of informative evidence, the greater the opportunity for the current extremum to be revised in favour of the correct alternative. Since such revision naturally grows rarer with time, the mechanism requires all available additional evidence with increasing durations in order to achieve the observed accuracy improvements, and since a bound effectively curtails this opportunity, the best fitting extremum model either has no bound (UExtE) or one set so high that it is never crossed (BExtE; see Figure S1 for bound crossing histograms). In the case of the BExtG model, trials with no bound crossing produce a random guess, and so a bound is required in conjunction with high drift rates to produce only correct bound crossings, only while informative evidence is present (Figure S1). In this way, the probability that at least one sample crosses the correct bound scales roughly linearly with duration, producing the observed, gradual accuracy improvements. Interestingly, while the bounded integration model estimated a bound level that produced many bound crossings, the benefit of its fit to the accuracy data was too small to warrant the additional complexity, according to the AIC metric. Thus, both the sequential sampling mechanism and the presence/absence of a decision bound remained inconclusive based on behaviour alone.

Decision-related Neural Signals and their Implications

To gain more insight into sensory and decision processes in this task, we examined neural signals that have been previously linked with three processing levels of perceptual decision-making (Heekeren et al., 2008), namely sensory evidence encoding (Figure 3A), evidence accumulation (Figure 3B), and motor preparation (Figure 3C).

The steady-state visual evoked potential (SSVEP), extracted at the flicker frequency of 18.75Hz, reflected encoding of the contrast difference between the correct (higher-contrast) and incorrect gratings (see Methods for details), thus tracking the sensory evidence for the decision (Figure 3A). This signal started at zero during the equal-contrast baseline, and stepped up to a level that varies with the contrast difference after evidence onset, falling back down to zero after evidence offset. The SSVEP traces remained relatively stable throughout the presentation of evidence, suggesting that a constant (i.e. non-adapting) drift rate is a reasonable simplifying model assumption.

Turning to the signatures of decision formation, the CPP exhibited a slow buildup and sustained elevation above baseline for lower contrast conditions, whereas for the high-contrast condition, it built steeply to an early, high-amplitude peak and dropped fully before the end of the stimulus period (Figure 3B). The ending CPP amplitude, measured in the 320 ms window ending at evidence offset, did not vary significantly across the four low-contrast evidence durations (rmANOVA, $F(3,45) = 1.23$, $p = 0.3$).

A long-established neurophysiological signature of motor preparation is the gradual suppression of spectral amplitude in the Mu/Beta (8-30 Hz) bands contralateral to the upcoming movement (Pfurtscheller & Da Silva, 1999). Evidence-dependent buildup dynamics during perceptual decisions have been commonly characterised in the lateralisation of this activity, reflecting relative motor preparation (Donner et al 2009; de Lange et al 2013; Murphy et al 2016). In the current task, Mu/Beta lateralisation, like the CPP, built more steeply in the high-contrast condition than in any low-contrast condition.

Unlike the CPP however, it did not return to baseline within the stimulus-evaluation period, instead sustaining through this period (Figure. 3c). In the low-contrast conditions, MBL built up to higher levels for longer evidence durations, (rmANOVA, F (3,45) =5.8, p=0.003; Post-hoc comparisons significant between 0.2s and 0.4s (*p=.003*), marginal between 0.4s and 0.8s (*p=.067*), and no significant effect between 0.8s and 1.6s (*p=0.7*).

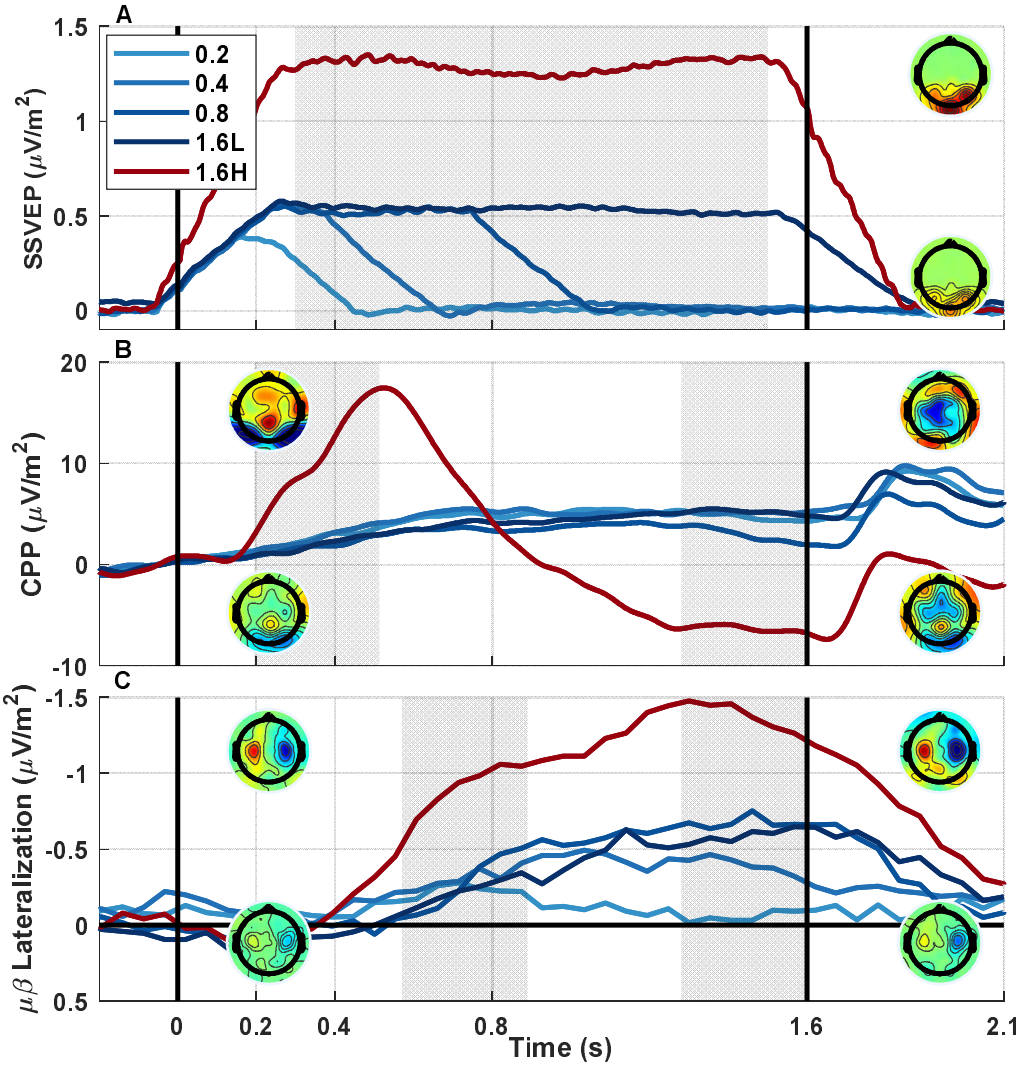

Figure 3. Neural Signals. (A) SSVEP showed a robust representation of sensory evidence encoding. Note that the signal ramps rather than suddenly steps simply due to the width of the window for spectral estimation (230 ms), and lags the physical contrast changes simply due to transmission delays to the visual cortex. Topographies show the average SSVEP amplitude from 300 ms to 1500 ms for the high contrast conditions (top) and the longest low contrast condition (bottom), with a primary focus at standard site Oz. (B) Event-related potential (ERP) at centroparietal sites averaged over trials (regardless of outcome) within each condition, showing that the centro-parietal positivity (CPP) undergoes a gradual buildup and sustained elevation for lower contrast conditions, and a peak at around 530 ms for the high contrast trials, at more than twice the amplitude. Topographies show ERP amplitude for the high contrast (top) and the average over low contrast conditions (bottom), for the time ranges 210-530 ms (left) and 1280-1600 ms (right). (C) Motor preparation was measured by subtracting ipsilateral from contralateral mu/beta-band activity (MB; 8-30 Hz) with respect to the correct side. The topographies show the difference between trials favouring a left minus right

response, again shown for both high contrast (top) and averaged low contrast (bottom) conditions in the windows 570-890 ms (left) and 1280-1600 ms (right).

An important distinction between the CPP and MBL lies in their basic signal properties. MBL is a subtraction between hemispheres and thus traces a differential decision variable whose sign indicates the favoured alternative; this means that noise variations favouring left/right alternatives tend to cancel each other in the average so that zero evidence produces zero lateralisation. In contrast, the CPP always builds positively, regardless of the favoured alternative, consistent with the sum of two underlying neural populations coding for the two alternatives. This means that noise variations do not cancel and the average CPP will exhibit a buildup even in conditions with weak or no evidence. This feature of the CPP blunts the distinction between noise-driven build-up and truly evidence-driven build-up for very weak evidence strengths (Steinemann et al., 2018), as seen here. Taking these distinct features of the CPP and MBL into account, the observed patterns are in principle consistent with a previously proposed accumulation-to-bound architecture (Kelly et al., 2021), in which cumulative evidence encoded at the CPP level is fed downstream to the motor preparation level reflected in mu/beta activity. As in previous research where responses were deferred until after stimulus offset (Twomey et al., 2016), the CPP's early peak in the high-contrast condition is consistent with the setting of a bound, which was more quickly and/or more often reached in the high-contrast trials than in the low-contrast trials. Whereas the accumulator at the CPP level falls immediately upon reaching the threshold, motor preparation signals sustain after decision commitment, in anticipation of the delayed cue for motor execution. However, while the early-peaking dynamics of the high-contrast CPP can rule out the unbounded models (Figure S2), there are implementations of the Extrema Detection models that could plausibly generate a building decision variable broadly resembling the CPP, which we consider next.

Neurally-constrained models

We devised a decision-signal generating mechanism for each of the three competing bounded models that could not be resolved based on behavioural modelling alone, in order to constrain them further by comparing simulated trial-averaged decision variable (DV) waveforms with observed CPP waveforms. All models generated sensory evidence from boxcar functions (stepping up during positive evidence) with added Gaussian noise as before (Figure 4A). Single-trial examples of the three DV schemes are shown in Figure 4B-D.

In the Integration model, the DV was computed as the perfect (lossless) integration of the momentary evidence samples over time (Figure 4B). Based on post-decision CPP dynamics observed in immediate response tasks and easy delayed-response conditions, we assumed that the decision variable falls back to baseline in a stereotyped way upon reaching the bound. For consistency with the non-integration models below, we modelled this fall-back as a quarter-sine wave (from peak to zero-crossing).

In the Extremum-tracking model, a running record of the most extreme evidence sample witnessed so far was encoded in the decision variable, with the same quarter-sine fall-down from the bound if and when it was crossed. In principle, this enables an early peak-and-fall in the high-contrast condition and a slower more sustained buildup in the low-contrast conditions (Figure 4C).

Finally, for the extrema detection model with guess default (BExtG), we simulated a DV involving no evidence-driven buildup dynamics on any single trial but rather a stereotyped

signal marking each single-trial bound crossing, which when averaged across trials could approximate a gradual buildup. In this “Extremum-flagging” model, we assumed that bound-crossings triggered a Half-Sine-shaped (upper half; (Weindel et al., 2025)) temporal function with an amplitude and width that was fixed across trials (Figure 4D), which would be expected to cluster at early latencies in high-contrast trials and spread over longer latencies in low-contrast trials, thus plausibly approximating the observed CPP dynamics. Though we use a neutral ‘flagging’ function here, the idea is consistent with classic theories of the closely-linked P300 or P3b component (O’Connell et al., 2012; Twomey et al., 2015), which posit that it reflects a process triggered by completion of a perceptual judgment, such as “context updating” (Polich, 2007) or response facilitation (Nieuwenhuis et al., 2005; Verleger, 2020). If no bound was reached by stimulus offset, there was no flag signal elicited, and the subject made a random guess.

As depicted in Figure 4B-D, the DVs in all models are treated as differential processes with a positive correct bound and negative error bound. However, to simulate CPPs, the absolute value of the differential DV was taken, under the assumption that the always-positive CPP reflects the sum of two neural populations coding cumulative evidence for each alternative in an exclusive way (one active at a time; following Afacan-Seref et al., 2018; Kelly et al., 2021). To constrain the models to produce CPP waveform dynamics, we added the mean-squared error (MSE) between the normalized real and simulated CPP as a “neural penalty term” alongside the G^2 metric quantifying the fit to behavioural accuracies in the objective function, with a range of weightings. To capture the relevant decision-signal dynamics, we extracted the time window from 200 ms (onset of contrast-dependent buildup) to 900 ms following evidence onset for the high-contrast average CPP, and from 200 ms to 1600 ms for the low-contrast CPPs, averaging across durations in the latter case. These waveforms were normalized by subtracting the first sample and dividing by the overall mean across both waveforms. We normalized simulated average decision variable trajectories in the same way and computed the mean-squared error between the two, weighting it by a variable factor to act as the neural penalty term.

In extracting the to-be-modelled CPP waveform starting at the onset of evidence-driven buildup, we remove the need to estimate transmission or other non-decision delays, which had also been unnecessary in behaviour-only modelling due to not fitting reaction time. Without loss of generality, we could therefore assume for simplicity that evidence accumulation and extremum-detection processes began without delay at evidence onset, and that the ‘flag’ signal began immediately upon bound crossing. It is important to note that this measure to remove unnecessary timing parameter estimation still allows for decision variable onset delays and flag-onset delays that may occur in reality. In all three models, we allowed the width of the sine-function describing the post-bound fall-down (quarter-sine) and flag (half-sine) to vary as a free parameter, on the basis that we cannot estimate these single-trial quantities from observed average waveforms without knowing bound-crossing times.

Although motor preparation signals were not used in the model fits, it was additionally of interest to simulate these signals from all models for qualitative comparison with mu/beta lateralisation (Figure 3C). To do this, we assumed that the relative motor preparation directly reflected the differential decision variable but with the distinction that it sustained at the level of the bound upon reaching it, rather than immediately falling like the CPP. From this perspective of motor preparation, the Extremum-flagging model can be considered highly similar in nature to the discrete stepping model proposed by Latimer et al., (2015), which

features stochastically occurring, discrete steps in neural activity reflecting transitions from an undecided to a decided state.

We comprehensively examined the relative ability of the three model classes to jointly fit accuracy and CPP dynamics by fitting not only the basic models with bound, drift rates and sine-width parameters, but also a range of plausible additional parameters, namely, drift rate variability, starting point variability, sequential sampling duration (allowing premature quitting), sampling onset time (allowing sampling to begin before or after evidence is available), collapsing bound, and in the case of integration, leakage (see methods for full explanation of each). We fit all models with five neural penalty term weightings (w = 0.1, 1, 10, 100, 1000) to examine how the behavioural and neural fits change as a function of emphasis placed on reproducing the CPP dynamics.

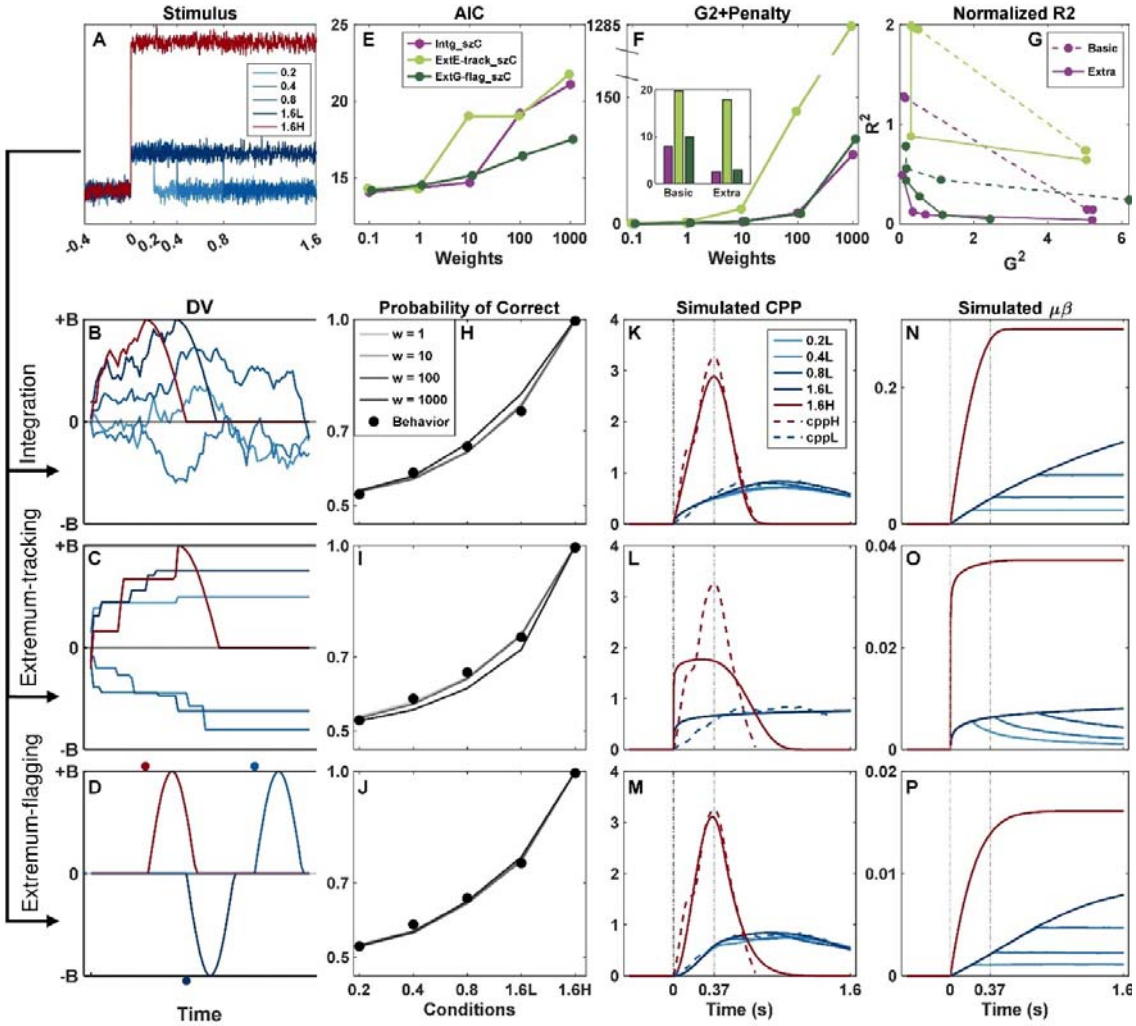

Figure 4. Neurally constrained models and their predictions. (**A**) Example evidence traces simulated for each of the five conditions. (**B-D**) single-trial examples of the decision variable in each of the three competing models, again simulating one trial per condition. (**B**) In the **Integration model,** the evidence was integrated over time until it reached a bound, after which it fell back to zero. Where the decision variable did not hit the bound the decision was made based on the sign of accumulated evidence at 1.6 sec. (**C**) In the **Extremum-tracking** model, the DV keeps track of the most extreme value so far, until it reaches the bound, after which it falls to zero. The sign of the extremum determined the choice, and the most extreme sub-bound value was used in the event that it did not

cross the bound. (**D**) In the **Extremum-flagging** model, an all-or-nothing Half-Sine-profile signal marking choice termination onsetting at the bound crossing time (see main text). As in the other models, one example DV trace per condition is shown; for three of these (red and two dark blue traces) the bound was reached, while in the others it was not, so no signal was generated (flat light blue lines), and the choice was made as a random guess. In all 3 models in this figure, starting point variability and collapsing bound parameters are included, and they have an equal number of free parameters. (**E**) Akaike's Information Criterion (AIC) derived from only the behavioural component of the neurally-constrained fit, plotted as a function of the weighting of CPP-waveform constraint. With increasing emphasis on neural data in the fit, the fit to behaviour was compromised to varying extents, and the Extremum-flagging model was best at retaining good behavioural fits at higher neural weights. (**F**) Overall neurally-constrained objective function (behavioural G^2 value plus weighted neural penalty quantifying divergence in observed vs simulated CPP) as a function of neural constraint weighting. The inset compares the objective function values with starting point variability and collapsing bound parameters (labelled 'Extra' in G) to the 'basic' models without either feature, at w = 10. (**G**) Neural fit (R^2) plotted against behavioural fit (G^2), illustrating a trade-off between how well the models can capture behaviour and the CPP up to w = 100. The closer the joint values come to the origin the better they are at simultaneously fitting both. (**H-J**) Predicted behavioural accuracy for a range of neural constraint weightings ('w'). (**K-M**) Simulated average CPP for the best fits of each model at a neural weighting of w=100 (see Figure S4 for simulations from all weightings, and Figure S5 for predicted bound crossing frequencies). The simulated average CPP (solid lines) is shown for all five conditions. The empirical data is also shown (dashed lines) with the waveforms for the four low-contrast conditions averaged together, as they were for the neurally-constrained fitting. (**N-P**) Simulated motor preparation. Same as (K-M) except showing the trial-averaged differential DV (without taking the absolute value) and having the signal sustain beyond bound crossing.

Among the models with various additional parameters, starting-point variability and collapsing bounds stood out as helping to achieve good CPP waveform fits without substantially sacrificing behavioural fits (Figure S3), and given that both of these features were exhibited empirically in motor preparation signal effects (see next section), we compare the three model classes in Figure 4E-P using models including both starting point variability and collapsing bounds (see Figures S6-S8 for basic versions of the models without the extra parameters). AIC derived from the behavioural fit element of the objective function generally increased with neural weighting (Figure 4E), demonstrating an expected tradeoff where the higher the emphasis on a close fit to CPP waveforms, the more the behavioural fit is compromised. Looking at the overall objective function (G^2 plus the neural penalty term; Figure 4F), the Extremum-tracking model clearly could not achieve a competitive fit, but the integration and Extremum-flagging models perform at a similar level. Although the integration model appeared to gain an advantage at extremely high neural constraint weightings (Figure 4F), this came with a greater sacrifice to behavioural fit (Figure 4E). We traced the neural-behavioural trade-off by plotting dissimilarity between simulated and observed data for the neural fit against the behavioural fit (Figure 4G). When endowed with starting point variability and collapsing bounds, both the Integration and Extremum-flagging model were able to achieve a better neural fit without sacrificing behavioural fit, compared to 'basic' versions of the models without those features. However, which of the two models gives the overall better fit depends on the relative importance one places on fitting behaviour versus neural dynamics. The average DV dynamics simulated from each model illustrate that these two models could both qualitatively produce average CPPs with a shallow incline and continued elevation that varied little across low-contrast durations, while also producing a steep initial rise and early peak in the high contrast condition (Figure 4K,M; Figure S4). By

contrast, the Extremum-tracking model could produce a peak-and-fall morphology in high-contrast, and sustained elevation in low-contrast conditions, but could not do so while retaining a gradual evidence-dependent buildup (Figure 4L, Figure S4). The estimated parameters and fit metrics for neural weight w = 100 are listed for these models in Table 2.

Table 2 Fit metrics and parameter estimates for neurally-constrained models with a neural-constraint weighting of w = 100. B refers to the bound; D1, D2 refers to the drift rates in the low- and high-contrast conditions. FlagWidth refers to the width of the half-sine while t0.5 and K refer to the semi-saturation constant and collapsing rate of the collapsing bound.

W = 100	G^2+Penalty	B	D1	D2	FlagWidth	ExtraParam	t0.5,K
BIntg	33.9	0.33	0.055	1.08	0.74	-	-
BIntg_szC	13.15	0.47	0.073	0.95	0.466	Sz = 0.32	t0.5 = 1.005, K = 1
BExtE	152.57	0.035	0.37	10.9	0.9	-	-
BExtE_szC	133.36	0.039	0.376	12.14	0.9	Sz = 0.00002	K = 0.99, T0.5 = 2.4
BExtG	54.23	0.0142	0.42	12.92	0.717	-	-
BExtG_szC	12.31	0.0152	0.4475	2.386	0.452	Sz = 0.00032	t0.5 = 2.47, K=0.4045

Relative motor preparation simulated from the best fitting parameters found in the CPP-constrained fits of all models exhibited dynamics that were qualitatively similar to the empirical MB lateralisation signal, including a steeper rise and higher sustained level for the higher contrast difference and greater amplitude variations across low-contrast durations than seen in the CPP. Temporal profiles varied across models, however: While both the integration and Extremum-flagging models, due to a high number of bound crossings, exhibited sustaining across the low contrast conditions (Figure 4N,P), similar to the empirical MB signal, the Extremum-tracking model showed a decrease beginning at evidence offset in each condition, since there were no bound crossings, and many trials would find a negative extremum arise by chance during the zero-evidence lead-out period (Figure 4O). The simulated motor preparation signals also highlight a notable aspect of the Integration model parameter estimates, which suggest a proportional difference in drift rates for high- vs low-contrast conditions (factor of 13) that is considerably greater than the physical contrast differences (40% vs 10%, i.e. a factor of 4); we return to this point in the discussion.

Motor Preparation

In the neural data analysis above, we examined relative motor preparation via Mu/Beta lateralisation, by subtracting activity ipsilateral minus contralateral to the correct hand (Donner et al., 2009). To examine Mu/Beta dynamics in more detail, we plotted the contralateral and ipsilateral Mu/Beta signals separately, broken out by decision outcome (correct/error; Figure 5). In immediate-response tasks, this analysis approach has previously revealed that the two competing motor alternatives race each other up to a stereotyped level

at the time of response that is invariant across stimulus conditions or reaction time (RT), indicating a fixed threshold associated with triggering the contralateral action (Corbett et al., 2023; Devine et al., 2019; Feuerriegel et al., 2021; Kelly et al., 2021; O'Connell et al., 2012). When evidence onset is anticipated, motor preparation reflected in Mu/Beta amplitude reduction contralateral to both hands has been found to begin building towards threshold even before evidence appears (Kelly et al., 2021), consistent with a dynamic 'Urgency' signal, defined as an evidence-independent buildup component that adds to cumulative evidence, gradually reducing the amount of cumulative evidence required to reach threshold and thus effectively implementing a collapsing decision bound (O'Connell et al., 2018). Moreover, fluctuations in pre-evidence mu/beta activity have been shown to predict trial-to-trial variability in choice and RT, in the way accumulator starting point variability does in models (Steinemann et al., 2018).

Here, despite the fact that the response had to be withheld until the post-stimulus response cue, MB-indexed motor preparation exhibited both of these effects. It rose significantly from -0.2 sec to 0 sec relative to evidence onset (main effect of time, $F(1,14) = 6.43$, $p = 0.02$), reflecting anticipatory urgency, before exhibiting evidence-dependent buildup after evidence onset, with contralateral preparation steepening in high-contrast trials, peaking at around 700 ms, and maintaining almost this level until the response period (Figure 5). In low-contrast trials, baseline levels of motor preparation already favoured the response that was eventually chosen before any evidence was presented (correctness x side interaction $F(1,14) = 8.85$, $p = 0.01$), reflecting significant starting-point variability that impacts eventual choice. Thus, despite the responses being deferred, MB activity traced the dynamics of the decision process from the outset of the evidence period, and exhibited effects consistent with decision process features whose inclusion in the models helped to achieve a good fit, namely starting point variability and a collapsing bound.

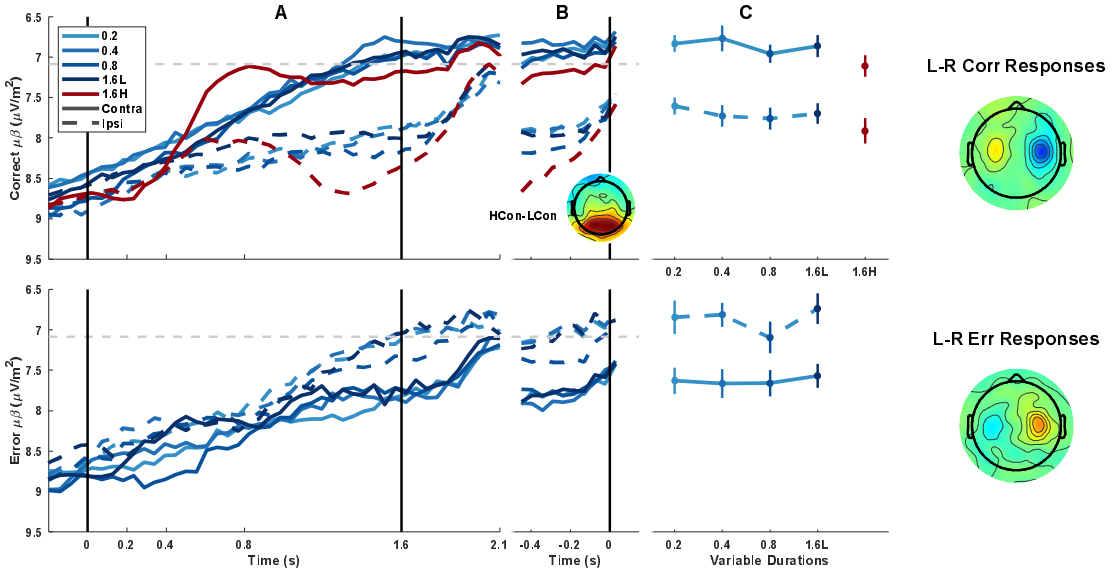

Figure 5. Mu/beta (MB) decreases reflecting building motor preparation, contralateral and ipsilateral to the correct response, in correct (top) and error trials (bottom), shown aligned to evidence onset (**A**) and response (**B**). Contralateral traces, on correct trials, and ipsilateral traces, on error trials, reach a fixed threshold prior to response. Interestingly, on easy, high-contrast trials, this threshold is reached at approximately 800 ms and sustains at just below that level until response which is marked by the grey dashed horizontal line to aid comparison of this preliminary peak to the ultimate peri-response level. (**C**) Amplitude of MB in 100 ms before the response for all 5 conditions. On high-contrast trials,

contralateral MB reached a less decreased level prior to response than it did on low-contrast trials. The topography inset in panel B shows the difference in MB between high-contrast and low-contrast conditions, revealing that this difference is unlikely motor-related, and more likely reflects greater attentional engagement in the harder low-contrast trials, known to be reflected in posterior alpha activity (Foxe & Snyder, 2011; Kelly & O'Connell, 2013). (D) Topographies of the amplitude difference between the trials with a brighter left-tilted minus right-tilted grating in 100ms prior to the response. The lateralisation, as expected, is reversed in error trials compared to the correct trials. Note that high-contrast trials were excluded from the error trials analysis due to lack of errors.

Discussion

Sequential sampling models have long been known to provide excellent quantitative fits to decision behaviour on diverse tasks (Ratcliff et al., 2016), but debates have persisted over whether decisions about continuously-presented, statistically stationary stimuli truly involve protracted sequential sampling, and whether the sampling process entails temporal integration specifically, as assumed by most models (Cisek et al., 2009; Ludwig et al., 2005; Stine et al., 2020; Uchida et al., 2006). The present study examined these questions in the case of a contrast-comparison task whose long, noiseless stimuli and delayed decision reports might seem to obviate protracted sampling, but whose subtle feature differences may be vulnerable to internal neural noise and hence benefit from protracted integration. This is a situation that, due to the absence of information on decision timing and the dominance of one fixed evidence strength, offers by itself very limited basis for adjudicating between alternative mechanisms using behaviour alone, and given the increasingly apparent task dependence of neural decision mechanisms (Okazawa & Kiani, 2023; Parés-Pujolràs et al., 2025; Shushruth et al., 2022), mechanisms in this task cannot simply be extrapolated from distinct task types such as immediate-response or expanded judgement tasks. Hence, to gather more information for model comparison while retaining the core task demands of interest, we manipulated the duration of the weak evidence without participants' awareness, and traced the average neural dynamics of decision formation in the centro-parietal positivity (CPP) and spectral EEG measures of motor preparation. We found convincing evidence for protracted sampling: accuracy steadily improved with evidence duration, including a substantial increase from 800 to 1600-ms duration, and in difficult trials the CPP, a signature of decision formation, remained elevated throughout the stimulus period. CPP dynamics also established the operation of a bound, which was reached early and often for the rare strong-evidence trials, but less frequently and later for the weak trials. At the motor preparation level, pre-evidence, baseline biases toward the ultimately chosen alternative indicated the operation of starting point variability, and dynamic anticipatory preparation suggested a collapsing bound effect. However, quantitative modelling revealed that although the addition of neural constraints did offer many more insights than was possible from behaviour alone, it could not identify one uniquely viable account of the data; specifically, when allowing for starting point variability and collapsing bounds, similarly close fits to both behaviour and CPP dynamics could be attained by an integration model and a non-integration model based on extremum detection.

Extremum detection models were proposed as accounts of decision behaviour decades ago (Watson, 1979), and although integration-based models such as the DDM have dominated behavioural modelling in the intervening years due to their mechanistic appeal and versatility, it was recently shown that these two accounts are surprisingly competitive in quantitatively explaining a range of important behavioural effects (Stine et al., 2020). Here, we went a step further by considering two ways that an extremum-detection model could

produce a gradual buildup in its trial-averaged decision variable dynamics, which could plausibly predict neural decision signal dynamics. One way, by continually tracking the most extreme sample encoded so far ('Extremum-tracking'), could fit behavioural data but could not simultaneously capture CPP dynamics because it predicts an initially steep and decelerating temporal profile that is not observed in the CPP (Figure 4L). A second way, in which a stereotyped signal flagged single-trial bound crossings that could produce gradual buildup when averaged, and which produced a guess if a bound was not crossed before stimulus offset ('Extremum-flagging'), could capture both behaviour and CPP dynamics to a degree comparable with Integration. When considering the implications of this, it is important to ask whether such a model could also fit data from immediate-response tasks. In discrete-trial, forced-choice tasks the response-locked CPP builds with a shallower slope and reaches a lower amplitude for weaker relative to stronger evidence, which in bounded accumulation frameworks is explained by evidence-dependent drift rates and a collapsing bound (Steinemann et al., 2018). The version of the Extremum-flagging model in the current study assumes a stereotyped signal triggered by each bound crossing and thus it should not show any such variation by evidence strength when aligned to the response; however, in principle, if one allowed for the possibility that the flag signal was smaller in amplitude and/or more temporarily jittered with respect to response execution for the weaker stimuli in which participants would have lower confidence, it could be possible to produce response-locked CPP waveforms that cross-over each other for high vs low evidence strength in the way that is observed. This will have to be explicitly tested in future work.

Both the Integration and Extremum-flagging models agreed on some key points: for example, they both support the operation of protracted sampling throughout the stimulus period when a bound was not reached, and both produced average decision signal dynamics that showed sustained elevation that was relatively invariant to duration, which in all cases resulted from the assumption that the scalp-measured CPP reflected the absolute value (i.e. rectified, always positive) of the underlying differential decision variable. However, there were also some notable differences, for example, in how parameter estimates and predictions changed as neural constraint weighting was increased. The Integration model began predicting later bound crossings beyond a neural constraint weighting of w=100 (Figure S5), while the Extremum-flagging model exhibited a stable pattern of correct- and error-bound crossings across all neural constraint weightings despite not producing any when based on behaviour alone (Figure S1). All models changed the relative drift rate estimates with increasing neural constraint weighting, but the Integration model predicted a particularly high ratio of drift rate for high versus low contrast, substantially greater than the ratio of the contrast itself (a factor of 4). Given that the onset of evidence was far more difficult to detect in low-contrast trials, compared to the strong bottom-salience of the evidence onset in easy trials, it is plausible that this drift rate ratio would indeed be greater than that of the physical contrast, but it is difficult to judge the plausibility of this degree of difference. The models were also quite different in the quantitative degree of starting point variability and collapsing bound that they estimated; for example, at a neural constraint weighting of w=100, the Integration model estimated starting point variability with a standard deviation 68% of the estimated bound, whereas the degree was much less (2%) in the Extremum-flagging model. Similarly the initial rate of bound collapse was 90%/sec in the Integration model (with gradual deceleration) compared to 16%/sec in the Extremum-flagging model. Meanwhile, both effects were strongly present in the observed motor preparation dynamics (Figure 5). The inferred operation of collapsing bounds is intriguing

from the point of view that responses were deferred in this task until after stimulus offset; however, given the prevalently weak evidence strength and tight 500-ms deadline after stimulus onset, it may be that subjects experienced urgency to commit to a choice in a timely fashion. Indeed, it has recently been shown that the dynamics of the Contingent Negative Variation in delayed response tasks is consistent with a cognitive-level urgency to terminate a decision even without the requirement of immediate response execution (McCone et al., 2025). The dynamics of Mu/Beta spectral amplitude during easy decisions further exhibited interesting features such as the initial rise of activity for the incorrect and ultimately chosen response alternative, inhibition during the main period of evidence-driven decision formation, and finally a fast buildup before the post-stimulus response, while the correct alternative reached approximately the threshold level already shortly after commitment was marked by CPP peaking early in the stimulus period. This suggests that the reaching of this threshold level in Mu/Beta may be necessary, but not in itself sufficient to trigger the action associated with the perceptual choice.

There are some noteworthy limitations to the neurally-constrained modelling methods. First, whereas we adopted a sensitivity analysis approach here where changes in the model fits were evaluated as a function of increasing emphasis on fitting the neural data, it should be possible in principle to instead weight the behavioural and neural data aspects in a data-driven way according to Bayesian principles where each information source is weighted according to uncertainty, i.e. EEG noise level. However, this noise-based weighting does not encompass theoretical importance, and it does not account for potential systematic biases, e.g. in an overlapping signal shifting the CPP waveform up or down, evidence for which we can see here in the neighbouring negativities. It was for this reason that our focus here was on which models could qualitatively capture the essential characteristics of the behaviour and waveforms, refraining from announcing a winner based on a small quantitative advantage. Another element of uncertainty that in principle could impact the relative quality of fit of the models pertains to the fall-down dynamics of the CPP once a bound is reached. While we have access to this in immediate response paradigms, we do not in delay-response paradigms and it is not clear that one can be readily extrapolated from the other. Aside from the uncertain shape of the fall-down, which in the case of integration could be linear rather than the sine-shaped function used here for consistency with the Extremum-flagging model, fall-down dynamics would also be affected by how immediately versus delayed it begins post-commitment (bound-crossing), and whether there is some amount of post-commitment accumulation as occurs in immediate-response tasks, all of which may have some impact on the morphology of the average waveforms.

Acknowledgments

H.H., K.S.M. and S.P.K. were supported by a Wellcome Trust Investigator Award (219572/Z/19/Z). R.G.O. was supported by Horizon 2020 European Research Council Consolidator Grant Ind Decision 865474.

Competing Interests

The authors declare no competing interests

Method

Data Collection

Participants

Sixteen healthy human participants (9 males, 4 females (aged 18-40); the gender of three participants was not recorded) were invited to take part in our experiment, which was approved by the Human Research Ethics Committee for the Sciences, University College Dublin in accordance with the Declaration of Helsinki. Sample size was not based on formal power analysis, but was close to similar EEG studies. All participants had normal or corrected to normal vision with no history of psychiatric diagnosis, sensitivity to flickering light, or head injury. Participants gave us written and informed consent and were compensated at €10 / hour. All together the participants completed 188 blocks of 80 trials (15040 trials in total).

Contrast Discrimination Task

Participants were instructed to perform a delayed-response, two-alternative forced choice contrast discrimination task, programmed using PsychToolbox-3 (Brainard & Vision, 1997; Kleiner et al., 2007; Pelli, 1997) in MATLAB and presented on a gamma-corrected 51 cm Cathode Ray Tube monitor (Dell E771p) with a refresh rate of 75 Hz and resolution of 1024 × 768. Participants were seated at a viewing distance of 57 cm inside a dark, sound-attenuated booth with their heads stabilized in a chin rest with forehead support and their left and right thumbs resting on the left and right buttons of a symmetrically shaped computer mouse, which formed the response alternatives. Eye position was monitored continuously throughout the experiment using a remote eye tracker (EyeLink 1000, SR Research, 1,000Hz).

Stimulus and procedure. The stimulus contained two interleaved grating patterns with a spatial frequency of 1 cycle per degree tilted at −45 and +45 degrees relative to the vertical meridian (Figure 1A), which flickered on and off in alternation, with each presented for one screen refresh on every 4th refresh, thus generating two phase-opposed steady-state visual evoked potentials at 18.75 Hz that cancel each other when contrasts are equal (see below). A central fixation dot (0.2^{o} diameter, grey) was presented, on which the participants fixated, followed 1200 ms later by the overlaid grating stimuli at 50% contrast (baseline period). After 600 ms of the baseline period, the fixation dot changed colour to yellow to warn the participants that evidence would be presented after another 600 ms. Evidence consisted of an equal-sized increment/decrement in the contrast of the two gratings such that one appeared brighter, which lasted for up to 1600 ms with the stimulus returning to baseline for shorter durations until the stimulus was finally removed at the end of the 1600 ms period. Participants were not aware that the duration of evidence would vary and believed it would always last 1600 ms. There were five equiprobable, randomly interleaved evidence conditions. In one easy condition, a high contrast difference (±40%, i.e., one grating 10% and the other 90%) was shown for the full 1600 ms, which served to reinforce the belief that evidence lasted for 1600 ms. The remaining four conditions consisted of a low contrast difference (±10%), which was presented for 200, 400, 800, or 1600 ms seconds. This contrast difference was difficult, with performance reaching 75% only on the longest duration trials (Figure 1B), and participants were not aware that the stimulus returned to baseline on the shorter duration trials, believing that all trials contained evidence for the full duration of

1600 ms (Figure 1A). This lack of awareness of variability in evidence duration is what differentiates our task from other variable-duration tasks (Kiani et al., 2008). Once the stimulus was removed, a go-cue instructed participants to indicate the higher contrast grating by clicking a mouse button with the thumb of the corresponding hand within 500 ms. Feedback was presented at the end of each trial in text and audio format. The text feedback informed the subjects whether they responded correctly ('Correct'), incorrectly ('Error'), prematurely (responded before the go-cue; 'Clicked too Early'), or missed the deadline of 500 ms to confirm their choice ('Too Late'). Although the short deadline was set on the response-cue to encourage the participants to indicate their decision immediately after the stimulus offset, since accuracy was the critical behavioural measure we analysed all responses up to 1 second after the go-cue. 0.4% of trials were missed (no button pressed up to 1 sec) and 2.6 % were premature responses (pressing before go-cue at stimulus offset), and these were excluded from calculating the accuracy. Participants received 10 points for correct, timely trials and 0 points for the other responses. At the end of each block, feedback was indicated on the mean accuracy and cumulative points gained during the block and participants were encouraged to attain as high a score as possible.

Training. Before performing the main experiment, participants conducted a practice version of the task to become familiar with the experiment and to be able to achieve the desired correct responses within the required deadlines. The training contained a series of short blocks of 20 trials with a fixed contrast difference shown for the full 1600 ms without any duration manipulation. The contrast difference started off with a high contrast difference of ±50%, dropping to ±20% with a 10% reduction in each block. They were required to achieve >90% in the easiest (±50%) and >70% in the hardest conditions (±20%), before progressing to the next difficulty level.

Statistical Analysis

Accuracies and response times were measured for each condition based on all trials with a valid response, which excluded 0.4% of trials that were missed (no response before 1s following the go-cue) and 2.6% of premature responses prior to the go-cue. Response times (RT) were recorded from the onset of evidence in milliseconds (ms).

One-way repeated measures analyses of variance (ANOVA) were carried out on the five task conditions, followed by pairwise comparisons (paired-sample t-tests), for RTs, accuracies, and neural amplitudes. For all statistical analyses, prior investigation was carried out to determine whether the data were suitable for parametric analysis by screening for any major violations of normality. Mauchley's test of sphericity was also conducted to assess the assumption of equal variances of the differences across all condition pairings in the rmANOVAs, and Greenhouse-Geisser corrections were applied when the sphericity assumption was violated.

EEG Acquisition and Preprocessing

Continuous EEG was acquired using a 128-channel ActiveTwo system (BioSemi) at a sample rate of 512 Hz. Vertical and horizontal eye movements were monitored using two vertical electrooculogram (EOG) electrodes placed above and below the left eye and two horizontal EOG electrodes placed at the outer canthus of each eye. Customized scripts in MATLAB (Mathworks, Natick, MA) and the EEGLAB toolbox (Delorme & Makeig, 2004) were used to analyse EEG data. EEG data were low-pass filtered by convolution with a 77-tap Hanning-windowed sinc function to give a 3-dB corner frequency of 38 Hz with strong attenuation at the mains frequency (50 Hz) (Widmann et al., 2015). Each block was

detrended quadratically. Noisy and flat-lined channels were identified by eye by comparing standard deviations to neighbouring channels and were interpolated based on surrounding channels using spherical splines. No high-pass filter was applied. Initially, EEG data were segmented into stimulus and response-aligned epochs. Stimulus-aligned epochs were extracted from stimulus onset to 960 ms after stimulus offset. All epochs were baseline-corrected relative to the interval of 106.6 ms pre-evidence onset (2 SSVEP cycles). We again applied spherical spline interpolation to any channel with excessively high variance with respect to neighbouring channels in each trial. Trials were rejected if an artifact occurred between evidence onset and stimulus offset (any channel with absolute magnitude >70 µV). One participant was excluded from EEG analyses due to excessive perspiration artifacts. Finally, to minimize the effects of volume conduction and avoid the possibility of overlapping signals confounding our interpretation of key signals such as the CPP (Kelly & O'Connell, 2013; Philiastides et al., 2014), a current source density (CSD) transformation was applied to each trial (Kayser & Tenke, 2006).

Electrophysiological data analysis

We extracted neural signatures of three processing levels of decision making: sensory evidence encoding, accumulation of evidence, and motor execution.

Neural signature of Sensory Evidence (Steady State Evoked Potential, SSVEP)

Flickering a stimulus at a certain frequency generates an oscillatory signal with the same frequency, known as the steady-state visual evoked potential (SSVEP), which provides a robust representation of physical contrast due to its narrow-band content (Regan, 1989). To obtain a direct measure of the sensory evidence upon which observers based their decisions (i.e. the relative contrast of the overlaid gratings) we generated a difference-SSVEP (d-SSVEP) by flickering the left- and right-tilted gratings in alternation at 18.75 Hz. This produced a signal that was zero, on average, for the equal-contrast baseline stimulus because the alternating gratings cancelled each other. When contrast differed, an aggregate d-SSVEP was produced with a phase dictated by the higher-contrast grating. The d-SSVEP signal was derived for each single trial by computing a Fourier Transform on untapered (boxcar) 320-ms time-windows (exactly 6 SSVEP cycles) in time-steps of 53.33 ms (1 cycle), and extracting the complex value representing oscillatory phase and magnitude at the 18.75-Hz frequency bin. We used the average complex oscillatory 18.75-Hz signal produced by the low-contrast 1600-ms condition to provide a common reference. This reference phase was calculated by trial-averaging the complex signal for the intermediate contrast level (S_{ref}). This was done independently for each electrode and time point. The angle of this resulting complex average was $\varphi_{ref} = \arg(S_{ref})$ then used as the reference phase to which all signal-trial data were aligned using phase rotation. Subsequently, these reference phases were subtracted from all trials, effectively rotating the phase data to correct for arbitrary offsets. One implication of the current approach is that we are unable to assess potential anticipatory modulations preceding the onset of the evidence. This means no reliable phase information is available for the pre-evidence period. However, this has minor concern in the current study, as our primary interest lies in modulations occurring during the evidence presentation. Oz electrode where the d-SSVEP was maximal on grand average was used to calculate this signal. The grand-average topography of the d-SSVEP was calculated by averaging from 300 ms to 1500 ms after stimulus onset (grey shading in Figure 3A) for the low-contrast, 1600-ms condition.

Neural signature of Evidence Accumulation (Centro Parietal Positivity)

Decision formation was examined by measuring the dynamics of the centro-parietal positivity (CPP), which has previously been shown to exhibit many properties predicted of evidence accumulation (O'Connell et al., 2012; Twomey et al., 2016). The evidence-locked CPP, baseline corrected to 106.6ms pre-evidence onset, was measured from a subset of electrodes chosen from a broad cluster of electrodes over centroparietal scalp (centred around Pz) at which the grand-average, high-contrast CPP was maximal at its peak latency (513 ms). 6 electrodes where the signal had the highest amplitude were selected from this cluster for each subject and the CPP was calculated by averaging these electrodes (see (Geuzebroek et al., 2023) for similar approach).

Motor Level decision threshold (Mu-Beta-Band spectral amplitude)

As in previous work (de Lange et al., 2013; Donner et al., 2009; Kelly & O'Connell, 2013; Steinemann et al., 2018), effector-selective motor preparation (Hanks & Summerfield, 2017; Kelly & O'Connell, 2015) was measured in the reduction of amplitude across the Mu/Beta bands (8-30 Hz) over the motor cortex (electrodes C3 and C4). Here, we calculated Mu/Beta amplitude using a short-time Fourier transform with a boxcar window size of 320 ms and time-steps of 53.33 ms, averaging across frequencies in the 8-30 Hz range but omitting 18.75 Hz to exclude the SSVEP. To produce a relative motor preparation signal that would reflect differential evidence for the decision, lateralized Mu/Beta was calculated by subtracting ipsilateral from contralateral amplitude, with respect to the hand corresponding to a correct answer on each trial. In the analysis of Figure 5, we computed average waveforms for correct and error trials separately, for the separate contralateral and ipsilateral signals without subtraction.

Model Fits to behaviour only

We explored five decision-making models, of which one was integration, three were extrema detection, and one was a snapshot strategy. Decisions in these models were made by applying a decision rule to samples of noisy momentary evidence taken from a normal distribution with a standard deviation of 0.1 arbitrary units, which acted as the scale reference point for all models. While noisy momentary evidence was constructed in the same way across all models, they differed in how a decision variable (DV) was formed from this evidence (Figure 2A). Core free parameters were common across models to enable direct comparisons of their fitting performance. These consisted of a separate "drift rate" for high and low contrast trials, dictating the strength of sensory evidence, and a "bound" parameter to set positive and negative criterion levels that the DV needed to reach to trigger a correct and incorrect decision, respectively.

All models were fit to the accuracies across the five experiment conditions (one 1600-msec high-contrast condition and four low-contrast conditions with durations of 200, 400, 800 and 1600 ms) by minimizing the χ^2 based statistic, G^2 (Ratcliff & Smith, 2004), described in detail below. The input sensory evidence signal for all models consisted of 1600 ms of Gaussian noise, plus a mean that stepped up and down according to a boxcar function during the periods of evidence to a height determined by the drift rate. To simulate accuracies across the five conditions, Monte-Carlo simulations of such trials were generated for a given set of parameter values and these parameters were optimized to match the empirical accuracies by minimizing the objective function (G^2) using a SIMPLEX algorithm (MATLAB's *fminsearch* function), generating a new Monte-Carlo simulation at each step of the optimization process. The G^2 statistic captured the difference in trial proportions between

the real and simulated data for each of the five conditions, and was calculated using the equation:

$$G^2 = 2n(\sum_{r=1}^{2}\sum_{c=1}^{5} p_{r,c} log \frac{p_{r,c}}{\pi_{r,c}})$$

Where n is the number of trials per condition, $p_{r,c}$ and $\pi_{r,c}$are the observed and predicted proportions of responses r (correct/error) for each of the five experimental conditions, c . Models with lower G^2 values fit the data more accurately.

The Akaike Information Criterion (AIC) was used to evaluate the goodness of fit (Kelly et al., 2021), calculated from G^2 using the equation:

$$AIC = G^2 + 2f$$

where f is the number of free parameters.

To minimize the risk that this fitting procedure would get stuck in a local minimum and fail to find the best-fitting parameters for a given model, we took three steps: 1) The G^2 was evaluated for a large grid of parameter vectors using 1000 simulated trials per parameter set, within the parameter limits listed in Table S4, with 10 points along each parameter dimension. 2) Next, we identified the grid points with the 10% best G^2 values for the models with up to 5 free parameters and the best 1000 grid points from the models with a higher number of free parameters, and ran the SIMPLEX algorithm with 20,000 trials per iteration starting from those parameter vectors. 3) Starting from the parameter vectors attaining the lowest G^2 in the previous step, the parameter estimates were refined by repeating each instantiation of the SIMPLEX algorithm with 100,000 trials per iteration, with the final parameter estimate and associated G^2 taken as the optimum. To facilitate the convergence of the SIMPLEX algorithm, the random number generator was set to the same seed at the start of each step. In a second step, we computed G2 Values from the parameter estimates of fits using 20,000 simulated trials per condition and a new random seed. This approach starting with a grid search has the advantage of ensuring a comprehensive exploration of the parameter space. We expanded the parameter value limits (Table S4) whenever the fits landed at the outer limit of the existing range.

Integration Models

We used a simple version of the well-known drift-diffusion model to implement temporal integration (Ratcliff). The samples of momentary evidence were integrated perfectly over time into a decision variable, DV(t), given by:

$$DV(t) = DV(t-1) + d(t) \times dt + N(0, s^2 dt)$$

where $d(t)$ is the drift rate at time t that was non-zero only for the duration of evidence, dt is the discrete time increment, and the last term refers to Gaussian noise with mean 0 and standard deviation of $s \times \sqrt{dt}$. Decisions were terminated by reaching the upper/lower bound or at stimulus offset if no bound was reached, in which case the decision was determined by the sign of the DV at that time (Figure 2A).

Three variants of this model were fitted, the first with only one drift rate applied equally to both high and low contrast-differences to provide a worst-case benchmark; the second with two separate drift rates (UIntg) and no decision bound so that choices were always determined at stimulus offset by the sign of the DV; and the third with a bound parameter included alongside the two drift rates (BIntg).

Extrema Detection models

Rather than accumulate evidence samples over time, extrema detection models compared each independent sample of momentary evidence to a criterion level, terminating upon the first sample to exceed it. The decision variable was thus given by

$$DV(t) = d(t) \times dt + N(0, s^2 dt)$$

Three variants of this Extrema Detection Model , were tested, differing only in how choice was determined when no bound was exceeded within the evidence period: i) by a random (50-50) Guess (ExtG; see Stine et al., 2020), ii) based on the sign of the last evidence sample (ExtL; stine), or iii) based on the sign of the most extreme (sub-bound) sample encountered throughout the evidence period. This third variant, labelled 'Extremum-tracking,' entailed a memory component to update the extrema as and when they were encountered throughout the trial, and like the Integration model, we tested three versions of this model with one drift rate and no bound, two drift rates and no bound, and two drift rates with a bound. Unbounded versions of the other two Extrema detection models were not implemented because, in the absence of a bound, they would trivially default to a random guess on all trials, or a decision based on just the last sample, which cannot provide accuracy improvements across the first 3 durations.

SnapShot with Guess

In this model, a single, randomly-selected sample of momentary evidence was used to determine the decision. In unbounded variants, the sign of this sample determined the choice regardless of its magnitude. In bounded variants, the sample determined the choice only if it exceeded the bound and a random guess was produced instead when the sample fell short of the bound. Again, three versions of this model were run, with one drift rate and no bound, two drift rates and no bound, and two drift rates with a bound.

Neurally-constrained Models

The models above were fitted to behaviour alone, and several of them captured accuracy equally well. To resolve this ambiguity, three of these successful models for which a means of producing buildup dynamics in the average decision variable could be conceived - the Integration model and two Extrema Detection models - were subsequently fitted jointly to behaviour and to the average CPP. To do this, a model-based simulation of the CPP was needed to compare to the empirical CPP. This simulation was derived in different ways in each model.

In the Integration model, the CPP was simulated as the absolute value of the decision variable (DV), representing differential cumulative evidence as previously described (Afacan-Seref et al., 2018). The use of the absolute value operator is based on the assumption that the CPP reflects the sum of two neural populations (one for each choice alternative) that activate in a mutually exclusive way to represent positive and negative values of the single, differential decision variable (Kelly et al., 2021). This is consistent with observations that the CPP builds with positive polarity regardless of choice and that the CPP reaches a stereotyped threshold level at response during urgency-free, continuous monitoring decisions, even though it derives from two accumulator processes only one of which ultimately triggers the decision (Kelly & O'Connell, 2013).

In the Extremum-tracking model, the CPP was simulated again as the absolute value of a differential DV, with the DV in this case being an iteratively-updated representation of the most extreme evidence sample encountered so far. In the final model based on Extrema

detection with a random Guess default, the decision variable is again the momentary evidence itself, subjected to bounds, but here it is assumed that a centroparietal signal is only evoked upon such bound crossings. We assumed that the trial-averaged CPP was the result of averaging single-trial discrete event waveforms that were triggered by, and therefore time-locked to, decision termination. We modelled this decision termination-flagging event as a half (upper) sinusoidal function whose width is a free parameter and whose amplitude is fixed, starting at the bound crossing time. When averaged, these half-sines can resemble any arbitrary waveform depending on the distribution of bound-crossing times. In theory, this formulation allows the Extrema Guess model to produce a signal with ramp-like properties similar to the CPP without accumulating evidence. For trials where no bound was reached, the CPP was simulated as zero throughout the evidence period. For consistency with this last, 'Extremum-flagging' model, the fall-down dynamics of the simulated CPP after each bound-crossing for the Integration and Extremum-tracking models was assumed to take the shape of a quarter-sine function (peak to zero-crossing), whose width was similarly set as a free parameter in the neurally-constrained fits. Note that the 'FlagWidth' parameter referred to half of the sinusoidal period across all 3 models for consistency, and so the actual duration of the peak-to-baseline fall-down in the Integration and Extremum-tracking models was half of the estimated value of this parameter.

Based on the above simulations of the CPP, neurally constrained models were implemented by combining behavioural fits (identical to those used in behaviour-only models) with a metric of CPP fit to derive a joint objective function to be optimized by the same SIMPLEX algorithm as used previously. Forming this combined objective function required a weighting to be assigned to the neural fit between simulated and empirical CPPs. Thus, the objective function was computed by adding a weighted penalty term to G^2

$$G_p^2 = G^2 + w((R_H)^2 + (R_L)^2)$$

$$R^2 = \frac{RSS}{TSS} = \frac{\sum_i^n (y_i - x_i)^2}{\sum_i^n (x_i - \underline{x})^2}$$

where R_H is the residuals sum of squares (RSS) over the total sum of squares (TSS) for the simulated, y_i, and empirical CPP, x_i, waveforms for the high contrast condition, and R_L is for the average waveform across low contrast trials. The low-contrast conditions were averaged so that the models would not be informed about amplitude variations across them, allowing these variations to be used as an independent evaluation of model fit. The neural weighting was set to each of the values $w = 0, 0.1, 1, 10, 100, 1000$ so that we could conduct a sensitivity analysis of how model fits varied with the degree of emphasis placed on the neural fit. To compute the neural R^2 term, we had to first apply appropriate time-windowing to exclude segments of the CPP waveform that did not clearly map onto the decision variable in the model, and normalize the real and simulated CPP so that they would have the same units. Specifically, we extracted windows of the observed CPP waveforms starting from 200 ms, the point at which the low and high-contrast CPP traces begin to diverge and presumably therefore the moment of initial impact of evidence, up to 900 ms in the high-contrast condition and up to 1600 ms in the low contrast conditions. The earlier end time for the high-contrast condition was chosen to avoid the bulk of a separate negative-going potential that appeared in the latter half of the stimulus-evaluation period in that condition, whose relationship to the decision process was not obvious and which would therefore risk biasing the measurement of the CPP during that time window. We then shifted the waveforms down so that they began at zero amplitude and then divided by the mean across

all sample points to normalize them. The same normalization procedure was applied to the model-simulated CPPs, which gave the simulated and empirical waveforms comparable units.

Beyond the core parameters of drift rate and bound, sequential sampling models are typically endowed with additional parameters to enable them to achieve a comprehensive behavioural fit (Ratcliff et al., 2016). We therefore explored a range of additional parameters and their impact on the neurally-constrained fits. Specifically, for each of the three model classes - Integration, Extremum-tracking and Extremum-flagging - we included one extra model feature at a time, alongside the two drift rates and bound of the basic model. We describe each additional feature in turn:

Sampling onset time (SampT). When sensory evidence is weak, it is difficult to distinguish evidence from noise and this can lead to variability in the onset time of sequential sampling (Devine et al., 2019). Though subtle, the CPP in this task appeared to begin to rise before the onset of evidence, suggesting a potentially early sampling onset (Figure 3B). SampT was a free parameter that was allowed to take a value before or after time zero, which in the models marked the time when informative contrast-difference evidence first became available for sampling. Figure S3 shows that this extra parameter did not substantively improve the fit of either of the competitive models.

Starting point variability (sz) Variability in the starting point of the decision variable allows for random trial-to-trial fluctuations in bias (Bogacz et al., 2006; Purcell et al., 2012). We implemented starting point variability as a uniform distribution of starting levels centred at the neutral position between the correct/error bounds whose standard deviation was the free parameter sz. Figure S3 illustrates that adding this extra parameter substantially improved the fit of the integration model. Interestingly, this nonzero starting-point variability is supported by the motor signal activity at the stimulus onset (Figure 5), although the model was not informed about this empirical effect.

Time-varying bound (κ,$t_{0.5}$) While constant bounds offer a parsimonious account of the decision criterion, bounds that change the criterion amount of evidence required for a decision as a function of elapsed time in the trial have been shown to better capture neural and behavioural data in certain cases, such as when urgency to respond is imposed through deadlines (Kelly et al., 2021), and although responses were deferred until after the long stimulus in the current task, a tight deadline of 0.5 sec was imposed at that point, which in combination with the predominant very weak evidence may have led to an experience of urgency. Such dynamically changing bounds have been shown to be optimal in certain circumstances involving unpredictable task difficulty (Malhotra et al., 2018) and are a critical feature of some extrema detection models (Thura et al., 2012). To determine whether models with time-varying bounds provide better fits to the data than models with fixed bounds, we implemented a time-varying bound using a hyperbolic ratio function, given by:

$$b(t) = \pm b_0 (1 - \kappa \frac{t}{t + t_{0.5}})$$

where b_0 is the initial boundary separation, time (t), κ represents the collapse rate, and $t_{0.5}$ the semi-saturation time. Note that this was assigned both a positive and negative value to correspond to the correct and incorrect alternative. This temporal function has been previously used to quantify the hypothetical urgency signal in physiological data (Churchland et al., 2008; Hanks et al., 2011; Voskuilen et al., 2016), except that the amount of collapse is expressed as a fraction of the total boundary separation rather than as an absolute value,

which simplified fitting and led to more interpretable parameter estimates. The nonlinear function provides flexibility to collapse more steeply initially and then gradually slow the collapse rate, allowing in this case for the fact that the two difficult levels are far apart, and that bounds need not collapse all the way to zero given that the models have default mechanisms to determine choice in the event of no bound crossing during the stimulus. Our results indicate that incorporating time-varying bounds improved the model fits for all the models (Figure S3). The optimal bound change for the two extrema-detection models was a collapsing bound although it was allowed to increase (Table S3&S4).

Between trial drift rate variability (eta) Although our stimulus does not include fluctuations in contrast, the internal representation of this contrast may fluctuate from trial to trial, with factors such as alertness and attention (Ratcliff et al., 2016). To allow for such between-trial variability in encoding sensory information, an extra parameter for trial-to-trial variability in drift rate was added, captured as Gaussian variability with standard deviation eta, centred on the drift rate parameters. This additional parameter improved the fit for integration model slightly (lower G^2+Penalty) while did not improve the fit for Extremum-flagging model (Tables S3, S5-8).

Accumulation duration (Dur) A central question in this study was whether judgements about prolonged static sensory evidence involve sequential sampling over the full evidence period, or only a portion of it. To explore this possibility in all three models, we implemented the models with one extra parameter ('Dur') that determined the time window starting from the onset of evidence encoding during which evidence was sequentially sampled for decision formation. The results revealed that the basic Integration model did improve with the addition of this duration parameter, but the estimate of this duration needed to fit the neural dynamics was less than 800 ms, therefore precluding reproduction of the significant increase in behavioural accuracy from the 800-ms to 1600-ms duration condition (Tables S3, S5-8).

Leaky accumulation. Another way that integration of evidence can be limited is through leak, whereby older samples are discounted in the cumulative total, and the decision variable gradually decays to zero in the absence of sufficient evidence. We implemented leaky accumulation through an additional leak parameter which scales-down the weighting of previous evidence relative to the current sample, according to:

$$DV(t) = (1 - leak) \times DV(t-1) + d(t) \times dt + N(0, s^2 dt)$$

The results demonstrated minimal information loss over time (leak = 0.0011 at w=100), with only a small benefit to fit from including the parameter, in agreement with previous findings of low leakage (Kiani et al., 2008).

The fitting procedure for the neurally-constrained models followed the same general strategy as the model fits to behaviour alone, starting with evaluation of objective function at each point of a comprehensive grid and running the SIMPLEX algorithm with the 10 best grid points as starting parameter vectors. In the most complex model, which extends the basic model by including starting point variability and a collapsing decision bound, five grid points were used for three parameters instead of 10 to limit computational expense (see Table S4). Running this procedure on all three model classes, we found that whereas the best objective function values for the Integration and Extremum-flagging models were 33.9 and 54.23, respectively (taking w=100 as representative), the best achieved by Extremum-tracking was 152.57. We therefore set Extremum-tracking aside and proceeded to refine the two competitive models, the best performing of which included both collapsing bound and

starting point variability. To further ensure convergence on global optima despite the additional complexity, we ran additional fits with starting vectors generated from the parameter estimates of models that had fewer free parameters. Specifically, for the 'szC' models (with free parameters for both collapsing bound and starting point variability), we started a fit from the best fitting 'C' model and with sz set to zero, half and equal of its estimated value in the 'sz' model. Analogously, we generated two more 'szC' starting vectors by taking the best fitting 'sz' model parameter values and adding an additional collapse rate equal to zero, equal to half and equal to the collapse rate found in the 'C' model.

References

Afacan-Seref, K., Steinemann, N. A., Blangero, A., & Kelly, S. P. (2018). Dynamic interplay of value and sensory information in high-speed decision making. *Current Biology*, *28*(5), 795–802.

Bogacz, R., Brown, E., Moehlis, J., Holmes, P., & Cohen, J. D. (2006). The physics of optimal decision making: A formal analysis of models of performance in two-alternative forced-choice tasks. *Psychological Review*, *113*(4), 700.

Brainard, D. H., & Vision, S. (1997). The psychophysics toolbox. *Spatial Vision*, *10*(4), 433–436.

Churchland, A. K., Kiani, R., & Shadlen, M. N. (2008). Decision-making with multiple alternatives. *Nature Neuroscience*, *11*(6), 693–702.

Cisek, P., Puskas, G. A., & El-Murr, S. (2009). Decisions in changing conditions: The urgency-gating model. *Journal of Neuroscience*, *29*(37), 11560–11571.

Corbett, E. A., Martinez-Rodriguez, L. A., Judd, C., O'Connell, R. G., & Kelly, S. P. (2023). Multiphasic value biases in fast-paced decisions. *Elife*, *12*, e67711.

de Lange, F. P., Rahnev, D. A., Donner, T. H., & Lau, H. (2013). Prestimulus oscillatory activity over motor cortex reflects perceptual expectations. *Journal of Neuroscience*, *33*(4), 1400–1410.

Delorme, A., & Makeig, S. (2004). EEGLAB: An open source toolbox for analysis of single-trial EEG dynamics including independent component analysis. *Journal of Neuroscience Methods*, *134*(1), 9–21.

Devine, C. A., Gaffney, C., Loughnane, G. M., Kelly, S. P., & O'Connell, R. G. (2019). The role of premature evidence accumulation in making difficult perceptual decisions under temporal uncertainty. *Elife*, *8*, e48526.

Donner, T. H., Siegel, M., Fries, P., & Engel, A. K. (2009). Buildup of choice-predictive activity in human motor cortex during perceptual decision making. *Current Biology*, *19*(18), 1581–1585.

Evans, N. J., & Wagenmakers, E.-J. (2020). Evidence accumulation models: Current limitations and future directions. *The Quantitative Methods for Psychology*, *16*(2), 73–90.

Feuerriegel, D., Jiwa, M., Turner, W. F., Andrejević, M., Hester, R., & Bode, S. (2021). Tracking dynamic adjustments to decision making and performance monitoring processes in conflict tasks. *Neuroimage*, *238*, 118265.

Foxe, J. J., & Snyder, A. C. (2011). The role of alpha-band brain oscillations as a sensory suppression mechanism during selective attention. *Frontiers in Psychology*, *2*, 154.

Geuzebroek, A. C., Craddock, H., O'Connell, R. G., & Kelly, S. P. (2023). Balancing true and false detection of intermittent sensory targets by adjusting the inputs to the evidence accumulation process. *ELife*, *12*, e83025.

Gold, J. I., & Shadlen, M. N. (2001). Neural computations that underlie decisions about sensory stimuli. *Trends in Cognitive Sciences*, *5*(1), 10–16.

Gold, J. I., & Shadlen, M. N. (2007). The Neural Basis of Decision Making. *Annual Review of Neuroscience*, *30*(1), 535–574. https://doi.org/10.1146/annurev.neuro.29.051605.113038

Hanks, T. D., Mazurek, M. E., Kiani, R., Hopp, E., & Shadlen, M. N. (2011). Elapsed decision time affects the weighting of prior probability in a perceptual decision task. *Journal of Neuroscience*, *31*(17), 6339–6352.

Hanks, T. D., & Summerfield, C. (2017). Perceptual decision making in rodents, monkeys, and humans. *Neuron*, *93*(1), 15–31.

Heekeren, H. R., Marrett, S., & Ungerleider, L. G. (2008). The neural systems that mediate human perceptual decision making. *Nature Reviews Neuroscience*, *9*(6), 467–479.

Heitz, R. P. (2014). The speed-accuracy tradeoff: History, physiology, methodology, and behavior. *Frontiers in Neuroscience*, *8*, 150.

Hyafil, A., de la Rocha, J., Pericas, C., Katz, L. N., Huk, A. C., & Pillow, J. W. (2023). Temporal integration is a robust feature of perceptual decisions. *Elife*, *12*, e84045.

Kayser, J., & Tenke, C. E. (2006). Principal components analysis of Laplacian waveforms as a generic method for identifying ERP generator patterns: I. Evaluation with auditory oddball tasks. *Clinical Neurophysiology*, *117*(2), 348–368.

Kelly, S. P., Corbett, E. A., & O'Connell, R. G. (2021). Neurocomputational mechanisms of prior-informed perceptual decision-making in humans. *Nature Human Behaviour*, *5*(4), 467–481.

Kelly, S. P., & O'Connell, R. G. (2013). Internal and external influences on the rate of sensory evidence accumulation in the human brain. *Journal of Neuroscience*, *33*(50), 19434–19441.

Kelly, S. P., & O'Connell, R. G. (2015). The neural processes underlying perceptual decision making in humans: Recent progress and future directions. *Journal of Physiology-Paris*, *109*(1–3), 27–37.

Khodadadi, A., & Townsend, J. T. (2015). On mimicry among sequential sampling models. *Journal of Mathematical Psychology*, *68*, 37–48.

Kiani, R., Hanks, T. D., & Shadlen, M. N. (2008). Bounded integration in parietal cortex underlies decisions even when viewing duration is dictated by the environment. *Journal of Neuroscience*, *28*(12), 3017–3029.

Kleiner, M., Brainard, D., & Pelli, D. (2007). *What's new in Psychtoolbox-3?* https://pure.mpg.de/rest/items/item_1790332/component/file_3136265/content

Lange, R. D., Chattoraj, A., Beck, J. M., Yates, J. L., & Haefner, R. M. (2021). A confirmation bias in perceptual decision-making due to hierarchical approximate inference. *PLOS Computational Biology*, *17*(11), e1009517.

Latimer, K. W., Yates, J. L., Meister, M. L. R., Huk, A. C., & Pillow, J. W. (2015). Single-trial spike trains in parietal cortex reveal discrete steps during decision-making. *Science*, *349*(6244), 184–187. https://doi.org/10.1126/science.aaa4056

Ludwig, C. J., Gilchrist, I. D., McSorley, E., & Baddeley, R. J. (2005). The temporal impulse response underlying saccadic decisions. *Journal of Neuroscience*, *25*(43), 9907–9912.

Malhotra, G., Leslie, D. S., Ludwig, C. J. H., & Bogacz, R. (2018). Time-varying decision boundaries: Insights from optimality analysis. *Psychonomic Bulletin & Review*, *25*(3), 971–996. https://doi.org/10.3758/s13423-017-1340-6

McCone, H., Devine, C. A., McNickle, E., Dully, J., Geuzebroek, A. C., McGovern, D. P., Kelly, S. P., & O'Connell, R. G. (2025). A Movement-Independent Signature of Urgency During Human Perceptual Decision Making. *bioRxiv*, 2025–05.

Nieuwenhuis, S., Aston-Jones, G., & Cohen, J. D. (2005). Decision making, the P3, and the locus coeruleus–norepinephrine system. *Psychological Bulletin*, *131*(4), 510.

O'Connell, R. G., Dockree, P. M., & Kelly, S. P. (2012). A supramodal accumulation-to-bound signal that determines perceptual decisions in humans. *Nature Neuroscience*, *15*(12), 1729–1735.

O'Connell, R. G., & Kelly, S. P. (2021). Neurophysiology of Human Perceptual Decision-Making. *Annual Review of Neuroscience*, *44*(1), 495–516. https://doi.org/10.1146/annurev-neuro-092019-100200

O'Connell, R. G., Shadlen, M. N., Wong-Lin, K., & Kelly, S. P. (2018). Bridging neural and computational viewpoints on perceptual decision-making. *Trends in Neurosciences*, *41*(11), 838–852.

Okazawa, G., & Kiani, R. (2023). Neural Mechanisms That Make Perceptual Decisions Flexible. *Annual Review of Physiology*, *85*(1), 191–215. https://doi.org/10.1146/annurev-physiol-031722-024731

Parés-Pujolràs, E., Kelly, S. P., & Murphy, P. R. (2025). Dissociable encoding of evolving beliefs and momentary belief updates in distinct neural decision signals. *Nature Communications*, *16*(1), 3922.

Pelli, D. G. (1997). The VideoToolbox software for visual psychophysics: Transforming numbers into movies. *Spatial Vision*, *10*(4), 437–442.

Pfurtscheller, G., & Da Silva, F. L. (1999). Event-related EEG/MEG synchronization and desynchronization: Basic principles. *Clinical Neurophysiology*, *110*(11), 1842–1857.

Philiastides, M. G., Heekeren, H. R., & Sajda, P. (2014). Human scalp potentials reflect a mixture of decision-related signals during perceptual choices. *Journal of Neuroscience*, *34*(50), 16877–16889.

Polich, J. (2007). Updating P300: An integrative theory of P3a and P3b. *Clinical Neurophysiology*, *118*(10), 2128–2148.

Purcell, B. A., & Palmeri, T. J. (2017). Relating accumulator model parameters and neural dynamics. *Journal of Mathematical Psychology*, *76*, 156–171.

Purcell, B. A., Schall, J. D., Logan, G. D., & Palmeri, T. J. (2012). From salience to saccades: Multiple-alternative gated stochastic accumulator model of visual search. *Journal of Neuroscience*, *32*(10), 3433–3446.

Ratcliff, R., & McKoon, G. (2008). The diffusion decision model: Theory and data for two-choice decision tasks. *Neural Computation*, *20*(4), 873–922.

Ratcliff, R., & Smith, P. L. (2004). A comparison of sequential sampling models for two-choice reaction time. *Psychological Review*, *111*(2), 333.

Ratcliff, R., Smith, P. L., Brown, S. D., & McKoon, G. (2016). Diffusion decision model: Current issues and history. *Trends in Cognitive Sciences*, *20*(4), 260–281.

Regan, D. (1989). Human brain electrophysiology. *Evoked Potentials and Evoked Magnetic Fields in Science and Medicine*. https://cir.nii.ac.jp/crid/1572543025661076864

Shushruth, S., Zylberberg, A., & Shadlen, M. N. (2022). Sequential sampling from memory underlies action selection during abstract decision-making. *Current Biology*, *32*(9), 1949–1960.

Steinemann, N. A., O'Connell, R. G., & Kelly, S. P. (2018). Decisions are expedited through multiple neural adjustments spanning the sensorimotor hierarchy. *Nature Communications*, *9*(1), 3627.

Stine, G. M., Zylberberg, A., Ditterich, J., & Shadlen, M. N. (2020). Differentiating between integration and non-integration strategies in perceptual decision making. *Elife*, *9*, e55365.

Thura, D., Beauregard-Racine, J., Fradet, C.-W., & Cisek, P. (2012). Decision making by urgency gating: Theory and experimental support. *Journal of Neurophysiology*, *108*(11), 2912–2930. https://doi.org/10.1152/jn.01071.2011

Trueblood, J. S., Heathcote, A., Evans, N. J., & Holmes, W. R. (2021). Urgency, leakage, and the relative nature of information processing in decision-making. *Psychological Review*, *128*(1), 160.

Twomey, D. M., Kelly, S. P., & O'Connell, R. G. (2016). Abstract and effector-selective decision signals exhibit qualitatively distinct dynamics before delayed perceptual reports. *Journal of Neuroscience*, *36*(28), 7346–7352.

Twomey, D. M., Murphy, P. R., Kelly, S. P., & O'Connell, R. G. (2015). The classic P300 encodes a build-to-threshold decision variable. *European Journal of Neuroscience*, *42*(1), 1636–1643. https://doi.org/10.1111/ejn.12936

Uchida, N., Kepecs, A., & Mainen, Z. F. (2006). Seeing at a glance, smelling in a whiff: Rapid forms of perceptual decision making. *Nature Reviews Neuroscience*, *7*(6), 485–491.

Verleger, R. (2020). Effects of relevance and response frequency on P3b amplitudes: Review of findings and comparison of hypotheses about the process reflected by P3b. *Psychophysiology*, *57*(7), e13542. https://doi.org/10.1111/psyp.13542

Voskuilen, C., Ratcliff, R., & Smith, P. L. (2016). Comparing fixed and collapsing boundary versions of the diffusion model. *Journal of Mathematical Psychology*, *73*, 59–79.

Waskom, M. L., & Kiani, R. (2018). Decision making through integration of sensory evidence at prolonged timescales. *Current Biology*, *28*(23), 3850–3856.

Watson, A. B. (1979). Probability summation over time. *Vision Research*, *19*(5), 515–522.

Weindel, G., Borst, J. P., & Maanen, L. van. (2025). Decision-making components and times revealed by the single-trial electro-encephalogram. *eLife*, *14*. https://doi.org/10.7554/eLife.108049.1

Widmann, A., Schröger, E., & Maess, B. (2015). Digital filter design for electrophysiological data–a practical approach. *Journal of Neuroscience Methods*, *250*, 34–46.

Wong, K.-F., & Wang, X.-J. (2006). A recurrent network mechanism of time integration in perceptual decisions. *Journal of Neuroscience*, *26*(4), 1314–1328.

Supplementary

Table S1 Pairwise comparisons of accuracy, showing a significant difference between each pair of consecutive durations

Duration 1	Duration 2	T	dof	p-value (uncorrected)
0.2s	0.4s	-3.78647	15	1.79×10^{-3}
0.4s	0.8s	-3.74	15	1.97×10^{-3}
0.8s	1.6s	-6.19855	15	1.70×10^{-5}

Table S2 Pairwise comparisons of mean RT. There was a significant difference in reaction time between each pair of consecutive durations except for the shortest durations (0.2s vs 0.4s).

Duration 1	Duration 2	T	dof	p-value (uncorrected)
0.2s	0.4s	1.40869	15	1.8×10^{-1}
0.4s	0.8s	17.8368	15	1.60×10^{-11}
0.8s	1.6s	2.49377	15	2.48×10^{-2}

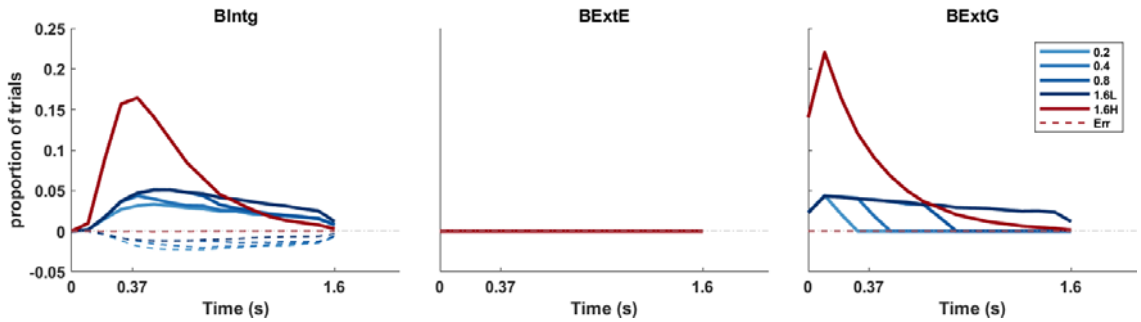

Figure S1. Histograms of Bound-crossing times per conditions in behaviour-only models that included a bound. The integration model, **BIntg**, allows 55-60% of trials to exceed the bound in the low-contrast conditions and nearly all trials in the high-contrast conditions, with the relative proportion of correct vs error bound crossing scaling with duration. In the **BExtE** model, the bound is set so high that it is never crossed, thus functioning in the same way as the unbounded model. This is because it can only achieve the full degree of accuracy improvement with duration when the opportunity for correct revision of the running extremum derives from the full remaining non-zero evidence. Bound crossings would reduce these revision opportunities. The **BExtG** model produces a good fit by setting a relatively high bound and assuming a drift rate for low-contrast conditions that is almost as high as the high-contrast condition. This produces no error bound crossings and an almost uniform distribution of correct bound crossing times during the evidence periods for hard trials, which produces a linearly increasing ratio of correct bound crossings to guesses across durations, in turn yielding a linear increase in accuracies.

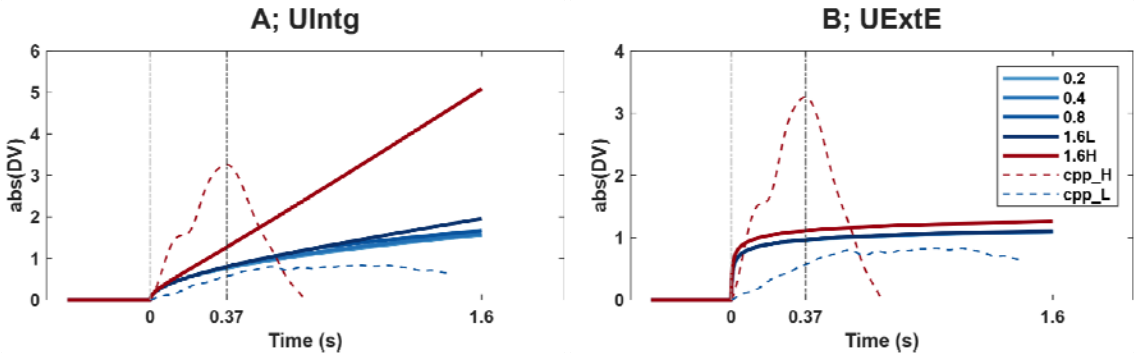

Figure S2 Simulated decision variable waveforms of the unbounded integration (A; UIntg) and non-integration (B; UExtE) models that produced good fits to behaviour alone, illustrating that neither of these models can reproduce the peak and falling-down of the empirical CPP signal (dashed) in the high-contrast condition. For consistency with the neurally-constrained modelling analysis, empirical traces show the mean CPP segments that are used as constraints, with low-contrast conditions averaged ('cppL;' See Neurally-constrained model-fitting in Results), whereas all five conditions are simulated for the models.

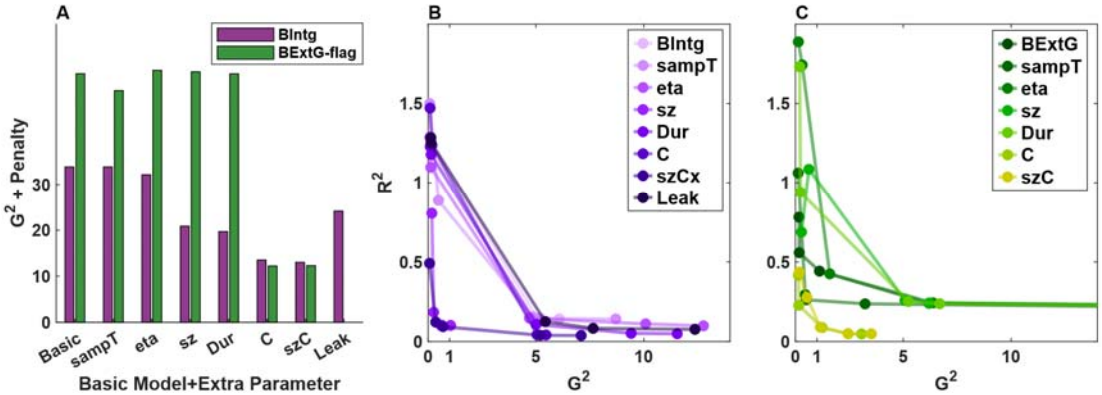

Figure S3 Impact of including additional, plausible free parameters to the basic neurally-informed, integration and non-integration models, taking the neural constraint weighting of 100 as a representative case. A) full objective function value (G^2+neural penalty term) across models at weighting of 100. For the integration models, both starting point variability ('sz') and the collapsing bound improved the fit, while the competitive Extremum-flagging model (BExtG-flag) underwent the greatest fit improvement with the addition of a collapsing bound. B,C) neural-behavioural fit plots illustrating the trade-off of fitting to both behaviour and the CPP for the additional-parameter models within each model class. For all models, the lowest weighting starts in the upper left part of the plot, and the trace moves downwards as better neural fits are achieved by weighting that aspect more, at some point curving rightwards as behavioural fit is compromised in favour of neural fit. B) The integration model including starting point variability achieved a better tradeoff in fitting jointly to behaviour and the CPP waveforms than any other single additional parameter (fit points reaching closer to origin). Additionally adding a collapsing bound achieves better neural fits (lower R^2) for high weightings, but at a cost to behavioural fit (G^2 exceeding 5 for higher weightings). C) For the Extremum-flagging model, a comparable trade-off was achieved, with good neural and behavioural fits, with the addition of a collapsing bound, and adding starting point variability to the collapsing bound model did not further improve the joint fit to behaviour and the CPP. "sampT" denotes the basic model with extra parameter as "sampling onset time"; similarly "eta" represents between-trial drift rate variability; "sz" indicates starting point variability; "Dur" corresponds to accumulation duration; "C" refers to models with a collapsing decision bound; "szC" represents models incorporating both starting point variability and a collapsing bound; and "Leak" denotes models with leaky accumulation.

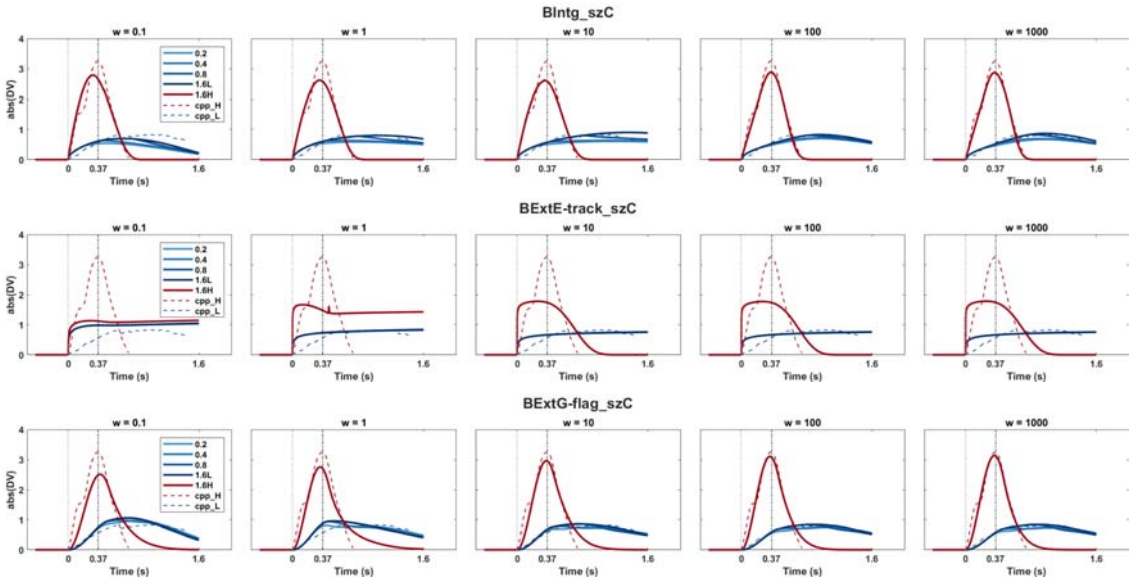

Figure S4 Simulated average CPP using the estimated parameters of the bounded Integration (top row), extrema-tracking (middle), and Extremum-flagging model (bottom) for the full range of neural constraint weightings, all with starting-point variability and collapsing bounds included (same models as shown in Figure 4).

Table S3 Neurally constrained Integration, Extremum-tracking and Extremum-flagging models with one extra parameter at neural constraint weighting **w = 100**. 'BIntg' refers to the bounded Integration model, 'BExtE' refers to Extremum-tracking, and 'BExtG' refers to Extremum-flagging which has a default guess. 'FlagWidth' refers to the width of half-sine while t05 and K are semi-saturation constant and collapsing rate parameters of the collapsing bound function.

W = 100	G^2+Penalty	B	D1	D2	FlagWidth	extraParam	t05, K
BIntg	33.9	0.33	0.055	1.08	0.74	-	-
BIntg_eta	32.19	0.5464	0.131	1.807	0.77	eta = 0.24	-
BIntg_sz	20.89	0.298	0.109	1.324	0.732	Sz = 0.59	-
BIntg_Dur	19.7	0.31	0.059	0.947	0.636	Dur = 0.73	-
BIntg_sampT	33.89	0.35	0.056	1.105	0.701	accT =0.004	-
BIntg_C	13.53	0.38	0.057	0.95	0.69	-	t0.5 =2.38, K =1.65
BIntg_szC	13.15	0.47	0.073	0.95	0.466	Sz = 0.32	t0.5 =1.005, K =1
BIntg_Leak	24.17	0.27	0.061	0.91	0.64	Leak=0.0011	-
BExtE	152.57	0.035	0.37	10.9	0.9	-	-
BExtE_szC	133.36	0.039	0.376	12.14	0.89	Sz =0.00002	t0.5 =2.49, K =1

BExtG	54.23	0.0142	0.42	12.92	0.717	-	-
BExtG_eta	54.9	0.0142	0.414	15.5	0.72	eta = 0.0005	-
BExtG_sz	54.6	0.0142	0.416	15.66	0.71	sz = 0.0003	-
BExtG_Dur	54.2	0.0141	0.4	14.3	0.72	Dur = 1.6	-
BExtG_sampT	50.5	0.0141	0.38	12.2	0.72	accT =0.006	-
BExtG_C	12.23	0.0152	0.45	2.4	0.44	-	t05 = 2.5, K = 0.4
BExtG_szC	12.31	0.0152	0.4475	2.38	0.452	Sz =0.00032	t0.5 = 2.47,K=0.404

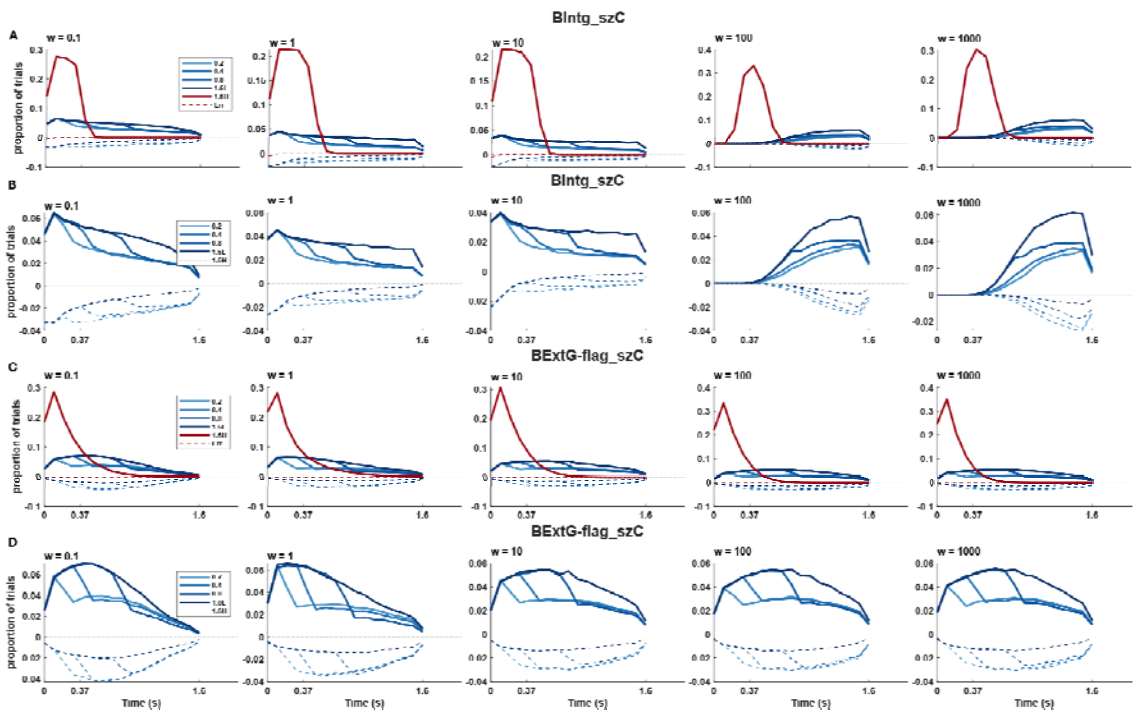

Figure S5. Bound crossing frequencies predicted by the Integration and Extremum-flagging models with starting-point variability and collapsing bounds. (**A**) bound crossing frequencies for all easy and hard trials of the Integration model, with a zoomed-in version of just the low-contrast conditions in (**B**) for better visibility. Error bound crossings are shown in dashed lines against the negative y-axis. In general, the overall proportion of hard trial with bound crossings decreased markedly with increasing neural constraint weighting for the Integration model, from approximately 0.95 at w=0.1 to 0.42 at w=1000. (**C & D**) bound crossings of the collapsing Extremum-flagging model. These decreased much less with increasing neural constraint weighting, from 0.92 at w=0.1 to 0.85 at w=1000.

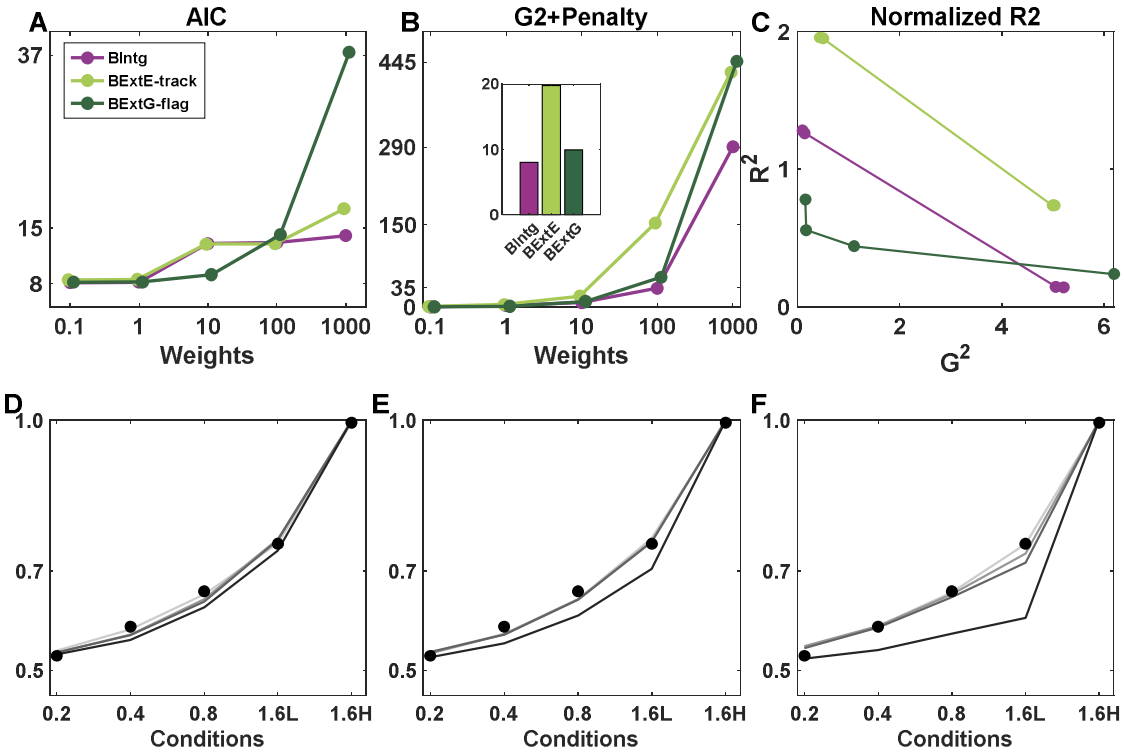

Figure S6 Neurally constrained for the basic models (**A**) Akaike's Information Criterion (AIC) derived from only the behavioural component of the neurally-constrained fit, plotted as a function of the weighting of CPP-waveform constraint. With increasing emphasis on neural data in the fit, the fit to behaviour was compromised to varying extents, and the Extremum-flagging model was best at retaining good behavioural fits at lower neural weights. (**B**) Overall neurally-constrained objective function (behavioural G^2 value plus weighted neural penalty quantifying divergence in observed vs simulated CPP) as a function of neural constraint weighting. For the visualisation purposes, the inset compares the objective function values to the 'basic' models at w = 10. The integration model outperforms at the neural weights w>1 (**C**) Neural fit (R^2) plotted against behavioural fit (G^2), illustrating a trade-off between how well the models can capture behaviour and the CPP up to w = 100. The closer the joint values come to the origin the better they are at simultaneously fitting both. (**D-F**) Predicted behavioural accuracy for a range of neural constraint weightings ('w') for (D) Integration (E) the Extremum-tracking and (F) the Extremum-flagging model.

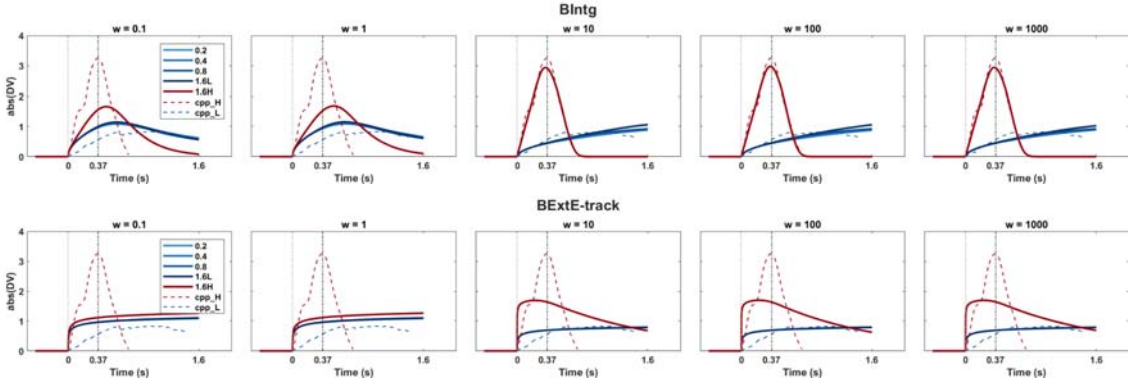

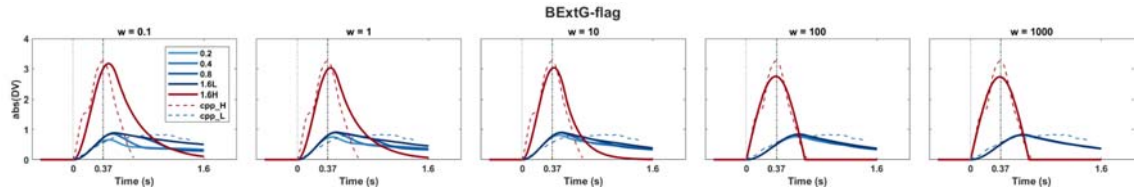

Figure S7 Simulated CPP signals for all basic models with no additional parameters beyond two drift rates and a constant bound, for each of the neural constraint weightings tested. The simulated waveforms over the neural weights depicted that the integration model, **BIntg**, and Extremum-flagging, **BExtG-flag**, qualitatively are successful in reproducing the CPP waveforms. The **BExtE-track** model sacrifices the fit to the easy condition to have a better prediction on the weak contrast conditions (The blue line fits better to the real CPP over the higher weights although the falling-down peak in the easy condition in red is not captured).

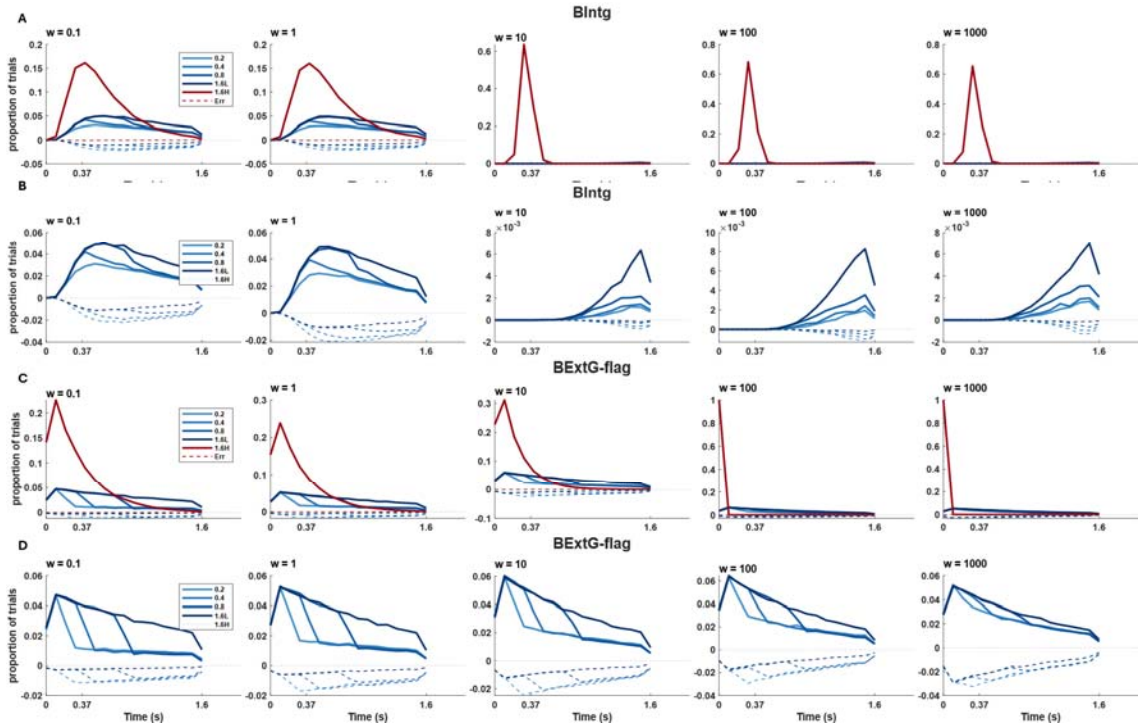

Figure S8 Bound crossing frequencies in correct and error trials of "basic" neurally constrained models with no additional parameters beyond two drift rates and a constant bound. (**A**) bound crossings of all easy and hard conditions for the Integration model. The portion of the hard trials crossing the bound decrease across the neural weights. In contrast, more easy trials are able to surpass the bound at higher neural constraint weightings. The drastic change occurred at w > 1. Further, the number of error trials reduces by focusing more on the neural weights. (**B**) The bound crossing of hard conditions in the bounded integration, Intg, is illustrated for better visibility. The bound crossing is delayed in the higher neural weights toward the later time in the trials. (**C**) Bound crossings for all conditions of the Extremum-flagging model. Similar to the integration model, a transition happened at w>1 where reproducing the early CPP peak improved. (**D**) A more visible pattern of bound crossing of ExtG-flag model in the hard conditions.

Table S4. parameters range; minimum and maximum values that each parameter can take in fminsearch. 'Inactive default values' indicate parameter settings used when the parameter is fixed rather than free. * showed the parameter with 5 grid points in the models with both starting point variability and a collapsing bound.

Parameters		Integration	ExtE-tracking	ExtG-flagging	Inactive Default values
bound	B	[0, 0.6*]	[0, 0.04]	[0, 0.04]	-
Drift rate (Low)	D1	[0, 0.6]	[0, 2]	[0, 7]	-
Drift rate (High)	D2	[0, 0.6]	[0, 15]	[0, 15]	-
Between trial Variability	eta	[0, 0.5]	[0, 0.5]	[0, 0.5]	0
Starting point*	sz	[0, 1]	[0, 0.04]	[0, 0.04]	0
Duration	Dur	[0.2, 1.6]	[0.2, 1.6]	[0.2, 1.6]	1.6
Accumulation onset Time	sampT	[-0.4, 0.4]	[-0.4, 0.4]	[-0.4, 0.4]	0
collapse*	k	[-5 5]	[-2, 2]	[-5 5]	0
Leak	leak	[0, 0.5]	-	-	0
FlagWidth	wd	-	-	[0.002, 0.9]	-
semi-saturation constant *	t05	[0.1 3]	[0.1 2.5]	[0.1 2.5]	-

Table S5 Neurally constrained Integration, Extremum-tracking and Extremum-flagging models with one extra feature at neural constraint weighting w = 0.1. 'BIntg' refers to the bounded Integration model, 'BExtE' refers to Extremum-tracking, and 'BExtG' refers to Extremum-flagging which has a guess default. 'FlagWidth' refers to the width of half-sine while t05 and K are semi-saturation constant and collapsing rate parameters of the collapsing bound function.

w = 0.1	G^2+Penalty	B	D1	D2	FlagWidth	ExtraParam	t05, K
BIntg	0.361	0.132	0.057	0.223	0.857	-	-
BIntg_eta	0.34	0.205	0.067	0.264	0.889	eta = 0.061	-
BIntg_sz	0.335	0.144	0.067	0.349	0.892	sz = 0.211	-
BIntg_Dur	0.344	0.173	0.059	0.23	0.456	Dur = 1.303	-
BIntg_sampT	0.375	0.245	0.063	0.242	0.517	sampT= 0.224	-
BIntg_C	0.387	0.535	0.057	0.221	0.868	-	t05 = 1.562, K = 2.001
BIntg_szC	0.166	0.289	0.122	1.367	0.878	sz = 0.578	t05 = 2.438, K = 2.044
BIntg_Leak	0.384	0.137	0.056	0.217	0.896	leak = 0.000	-

BExtE	0.837	0.035	0.388	1.631	0.004	-	-
BExtE_szC	0.704	0.026	0.408	1.932	0.891	sz = 0.031	t05 = 2.1; K = -0.62
BExtG	0.32	0.015	0.837	2.147	0.537	-	-
BExtG_eta	0.513	0.02	2.772	4.133	0.672	eta = 0.1	-
BExtG_sz	0.419	0.015	0.69	2.336	0.702	sz = 0.003	-
BExtG_Dur	0.54	0.019	2.807	4.186	0.562	Dur = 1.501	-
BExtG_sampT	0.338	0.016	1.052	4.671	0.709	sampT = -0.043	-
BExtG_C	0.22	0.015	0.405	1.789	0.511	-	t05 = 2.299; K = 0.401
BExtG_szC	0.26	0.015	0.502	2.05	0.498	sz = 0.003	t05 = 2.354; K = 0.512

Table S6 Neurally constrained Integration, Extremum-tracking and Extremum-flagging models with one extra feature at neural constraint weighting **w = 1**. 'BIntg' refers to the bounded Integration model, 'BExtE' refers to Extremum-tracking, and 'BExtG' refers to Extremum-flagging which has a default guess. 'FlagWidth' refers to the width of half-sine while t05 and K are semi-saturation constant and collapsing rate parameters of the collapsing bound function.

w = 1	**G^2+Penalty**	**B**	**D1**	**D2**	**FlagWidth**	**ExtraParam**	**t05, K**
BIntg	2.673	0.134	0.056	0.223	0.866	-	-
BIntg_eta	2.324	0.178	0.069	0.274	0.624	eta = 0.064	-
BIntg_sz	0.628	0.189	0.085	0.95	0.897	sz = 0.372	-
BIntg_Dur	2.5	0.162	0.059	0.236	0.587	Dur = 1.274	-
BIntg_sampT	2.26	0.19	0.069	0.659	0.9	sampT = -0.4	-
BIntg_C	2.652	0.15	0.056	0.225	0.864		t05=1.36;K=0.3
BIntg_szC	0.598	0.287	0.109	1.128	0.655	sz = 0.573	t05=3.8;K= 1.42
BIntg_Leak	2.642	0.135	0.056	0.224	0.819	Leak = 0	-
BExtE	4.413	0.034	0.387	1.642	0.18	-	-
BExtE_szC	2.055	0.039	0.515	11.031	0.885	sz = 0.04	t05=1.8;K=-1.86
BExtG	1.294	0.015	0.66	1.959	0.5	-	-
BExtG_eta	3.802	0.02	2.748	4.593	0.587	eta = 0.498	-

BExtG_sz	2.794	0.017	1.513	4.58	0.9	sz = 0.009	-
BExtG_Dur	2.115	0.016	1.037	2.37	0.527	Dur = 1.475	-
BExtG_sampT	1.041	0.014	0.531	12.684	0.746	sampT =-0.01	-
BExtG_C	0.61	0.015	0.429	1.804	0.374	-	t05=2.44;K= 0.4
BExtG_szC	1.088	0.015	0.662	2.288	0.443	sz = 0.004	t05=2.48;K=0.4

Table S7 Neurally constrained Integration, Extremum-tracking and Extremum-flagging models with one extra feature at neural constraint weighting **w = 10**. 'BIntg' refers to the bounded Integration model, 'BExtE' refers to Extremum-tracking, and 'BExtG' refers to Extremum-flagging which has a guess default. 'FlagWidth' refers to the width of half-sine while t05 and K are semi-saturation constant and collapsing rate parameters of the collapsing bound function.

w = 1	**G^2+Penalty**	**B**	**D1**	**D2**	**FlagWidth**	**ExtraParam**	**t05, K**
BIntg	7.99	0.36	0.06	1.1	0.67	-	-
BIntg_eta	7.63	0.36	0.06	1.15	0.73	eta = 0.05	-
BIntg_sz	2.69	0.3	0.10	1.34	0.75	sz = 0.6	-
BIntg_Dur	7.17	0.34	0.06	1.08	0.74	Dur = 1.15	-
BIntg_sampT	7.94	0.37	0.06	1.1	0.63	samp =-0.09	-
BIntg_C	5.9	0.4	0.06	0.95	0.66	-	t05=2.14;K=1.6
BIntg_szC	2.56	0.3	0.11	1.21	0.66	sz = 0.6	t05=4;K = 0.8
BIntg_Leak	7.93	0.3	0.06	1	0.77	Leak = 0	-
BExtE	19.76	0.03	0.38	10.9	0.9	-	-
BExtE_szC	17.87	0.04	0.38	12.32	0.9	sz = 0	t05=2.5;K=0.9
BExtG	9.96	0.01	0.51	2.07	0.52	-	-
BExtG_eta	10.1	0.01	0.47	2.22	0.57	eta = 0.083	-
BExtG_sz	10.26	0.01	0.47	10.2	0.73	sz = 0	-
BExtG_Dur	10.27	0.01	0.46	15.4	0.72	Dur = 1.57	-
BExtG_sampT	5.75	0.01	0.49	15.7	0.72	sampT=-0.01	-
BExtG_C	2.99	0.015	0.46	2.11	0.43	-	t05=2.03;K=0.3
BExtG_szC	2.96	0.015	0.45	2.16	0.45	sz = 0	t05=2.16;K=0.3

Table S8 Neurally constrained Integration, Extremum-tracking and Extremum-flagging models with one extra feature at neural constraint weighting **w = 1000**. 'BIntg' refers to the bounded Integration model, 'BExtE' refers to Extremum-tracking, and 'BExtG' refers to Extremum-flagging which has a guess default. 'FlagWidth' refers to the width of half-sine while t05 and K are semi-saturation constant and collapsing rate parameters of the collapsing bound function.

w = 1000	G^2+Penalty	B	D1	D2	FlagWidth	ExtraParam	t05, K
BIntg	290.87	0.34	0.05	1.07	0.716	-	-
BIntg_eta	210.09	0.62	0.15	2	0.772	eta = 0.312	-
BIntg_sz	203.28	0.3	0.11	1.33	0.744	sz = 0.6	-
BIntg_Dur	109.65	0.312	0.07	0.95	0.656	Dur = 0.672	-
BIntg_sampT	292.67	0.343	0.04	1.05	0.686	sampT =-0.01	-
BIntg_C	87.94	0.451	0.06	0.95	0.704		t05=0.6;K=0.9
BIntg_szC	82.17	0.56	0.1	1.02	0.2	sz = 0.425	t05=3.9;K =2.35
BIntg_Leak	165.4	0.36	0.08	0.86	0.006	Leak =0.002	-
BExtE	1476.26	0.03	0.29	10.81	0.9	-	-
BExtE_szC	1284.31	0.04	0.31	12.31	0.9	szC = 0	t05 = 2.5; K=0.9
BExtG	446.2	0.01	0.19	15.91	0.714	-	-
BExtG_eta	450.33	0.01	0.18	13.87	0.718	eta = 0.006	-
BExtG_sz	446.7	0.01	0.17	15.22	0.718	sz = 0	-
BExtG_Dur	448.17	0.01	0.2	14.37	0.716	Dur = 1.576	-
BExtG_sampT	444.29	0.01	0.23	8.57	0.717	sampT=-0.00	-
BExtG_C	97.707	0.01	0.47	2.474	0.467	-	t05 =2.49;K=0.4
BExtG_szC	100.37	0.01	0.46	2.471	0.467	szC = 0	t05=2.49;K =0.4